STUDIES OF LEAD-FREE FERROELECTRIC MATERIALS DERIVED FROM THE $AgNbO_3$-BASED SOLID SOLUTION SYSTEMS

by

Chia-Yin (Allen) Wei
B. Sc., Simon Fraser University, 2006

THESIS SUBMITTED IN PARTIAL FULFILLMENT OF
THE REQUIREMENTS FOR THE DEGREE OF

MASTER OF SCIENCE

In the
Department of Chemistry

SIMON FRASER UNIVERSITY

Spring 2010

APPROVAL

Name: Chia-Yin (Allen) Wei

Degree: Master of Science

Title of Thesis: Studies of Lead-Free Ferroelectric Materials Derived from the $AgNbO_3$-based Solid Solution Systems

Examining Committee:

Chair

Dr. Paul Li
Associate Professor, Department of Chemistry

Dr. Zuo-Guang Ye
Senior Supervisor
Professor, Department of Chemistry

Dr. Charles Walsby
Supervisor
Assistant Professor, Department of Chemistry

Dr. Michael Eikerling
Supervisor
Associate Professor, Department of Chemistry

Dr. Hua-Zhong Yu
Internal Examiner
Professor, Department of Chemistry

Date Defended/Approved: **Friday, April 16, 2010**

Declaration of
Partial Copyright Licence

ABSTRACT

The lead-free ferroelectric materials, (1-*x*)$AgNbO_3$-*x*$KNbO_3$ (AN-KN) and (1-*x*)$AgNbO_3$-*x*$K_{0.5}Na_{0.5}NbO_3$ (AN-KNN) solid solutions were prepared in the form of ceramics by solid state reaction under controlled O_2 atmosphere. The structure and properties of these two systems have been systematically investigated. The electric study of the AN-KN and AN-KNN ceramics suggests that the dielectric, ferroelectric, and piezoelectric properties in AN are improved significantly by the substitution of KN and KNN, indicating that these materials are promising for a wide range of applications such as ceramic capacitors, electromechanical transducers, and non-volatile memory devices. Such enhanced properties are attributed to the induced normal ferroelectric state in AN–based solid solutions. The crystal structural analysis of 0.80AN-0.20KNN confirms that the initial centrosymmetric and nonpolar phase (Pbcm) of AN has been transformed into a non-centrosymmetric and polar symmetry $Pbc2_1$.

ACKNOWLEDGEMENTS

I would like to express my sincere appreciation to my senior supervisor, Dr. Z.-G. Ye, for giving me the opportunity to work in his lab, and for his helpful guidance, continuous support and encouragement throughout these years of my graduate study.

I would also like to thank my supervisory committee members, Dr. Michael Eikerling and Dr. Charles Walsby, for their valuable advice and suggestions during the course of this work.

I extend my thanks to Dr. Hogan Yu for accepting to be the internal examiner of my thesis.

I am very grateful to all former and present members of our research group, for providing me with help, support and friendship. Especially, I would like to thank Mr. Hamel Tailor and Dr. Chao Lei for their great help and supportive suggestions.

I would like to express my thanks to the members of Department of Chemistry for their support.

The financial supports from the Department of Chemistry, Simon Fraser University, the Natural Sciences and Engineering Research Council of Canada, and the U. S. Office of Naval Research are greatly appreciated.

Finally, I would like to express my deepest gratitude to my parents for their unconditional love, constant support and encouragement.

TABLE OF CONTENTS

LIST OF FIGURES

LIST OF TABLES

LIST OF ABBREVIATIONS

AN	$AgNbO_3$
BT	$BaTiO_3$
d_{33}	piezoelectric coefficient
ε'	real part of permittivity
ε''	imaginary part of permittivity
ε_m	maximum dielectric constant
ε_{rt}	room temperature dielectric constant
KN	$KNBO_3$
KNN	$(K_{0.5}Na_{0.5})NbO_3$
k_p	electromechanical coupling constant
MPB	morphotropic phase boundary
P_s	spontaneous polarization
P_r	remnant polarization
PMN-PT	$Pb(Mg_{1/3}Nb_{2/3})O_3$-$PbTiO_3$
PZT	$PbZrO_3$-$PbTiO_3$
tan δ	dielectric loss
T_C	Curie temperature
$T_{T\text{-}O}$	tetragonal to orthorhombic phase transition temperature
XRD	x-ray diffraction

Chapter 1

General Introduction

Ferroelectric and piezoelectric materials are widely used in modern technology for applications in information storage, communication, navigation, and medical diagnosis and treatment [1]. According to the chemical composition and physical morphology, ferroelectric and piezoelectric materials can be divided into four categories: ceramics, single crystals, polymers, and composite materials. Among these, ceramics are the most commonly used in industry because they are relatively inexpensive and easy to prepare. This chapter introduces some basic concepts and background information related to this thesis work, including ferroelectricity, piezoelectricity, ceramic sintering, perovskite structure, and lead-free materials.

1.1 Piezoelectricity

Piezoelectricity is defined as the coupling between a material's electrical and mechanical effects. Piezoelectric materials can exhibit both the direct piezoelectric effect and the converse piezoelectric effect. For the direct piezoelectric effect, the electric polarization is induced proportionally to an applied mechanical stress. Figure 1.1 shows

the mechanism of the direct piezoelectric effect. When a pressure is applied to a piezoelectric material, the magnitude of polarization (P) decreases. Conversely, if a tensile force is applied to the same materials, P increases. The effect can be expressed by the following equation:

$$D_i = d_{ij} T_i \,, \tag{1.1}$$

where D_i is the induced charge density, T the stress, and d_{ij} the piezoelectric coefficient. Conversely, when the strain of the material is changed under application of an electric field , it is called the converse piezoelectric effect, which can be expressed by:

$$S_j = d_{ji} E_j \,, \tag{1.2}$$

where S_j is mechanical strain, E_j the electric field, and d_{ji} the piezoelectric coefficient tensor [2].

In both the direct and converse piezoelectric effects, the piezoelectric coefficient varies in different directions in a material. For example, d_{33} indicates that a stress applied in the direction 3 will produce an electric polarization along the same direction, or vice versa, i.e.

$$D_3 = d_{33} T_3 \,, \tag{1.3}$$

$$S_3 = d_{33} E_3 \,, \tag{1.4}$$

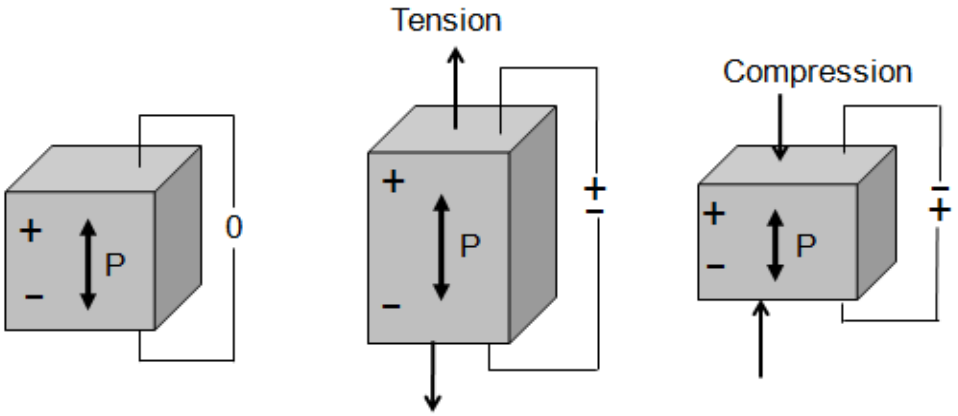

Figure 1.1: The mechanism of the direct piezoelectric effect (adapted from Ref.[3]). When the piezoelectric materials are compressed or pulled, the change of magnitude of polarization (P) in the materials generates an electric charge on the opposing faces.

1.2 Ferroelectricity

Ferroelectrics are polar dielectrics, which possess a spontaneous polarization in the absence of an external electric field. The direction of the spontaneous polarization can be switched between the symmetry-equivalent states by an application of an external electric field [4]. It has been known that the spontaneous polarization disappears when the temperature increases above well-defined temperature, called the Curie temperature (T_C). At temperatures above T_C, the material is in paraelectric state for which the material adopts a centrosymmetric non-polar structure and thereby no ferroelectricity is exhibited in the material. A decrease in the temperature below T_C results in a structural phase

transition of the paraelectric structure to form a non-centrosymmetric polar structure, in which the displacements of cations and anions give rise to the spontaneous polarization. Since the lattice symmetry in the ferroelectric phase is always lower than that in the paraelectric phase, there are more than one possible polarization states in the ferroelectric phase. Figure 1.2 shows the minima of two possible polarization directions separated by a potential energy barrier (ΔE) in a double-well energy diagram when the temperature is below T_C. Conversely, when the temperature is above T_C, there is only one minimum, because the materials are nonpolar in the paraelectric state. In the ferroelectric state, the interaction energy of adjacent dipoles is minimal if the dipoles align themselves parallel along a common direction in a certain region. Such a region with a uniform polarization direction is called a ferroelectric domain.

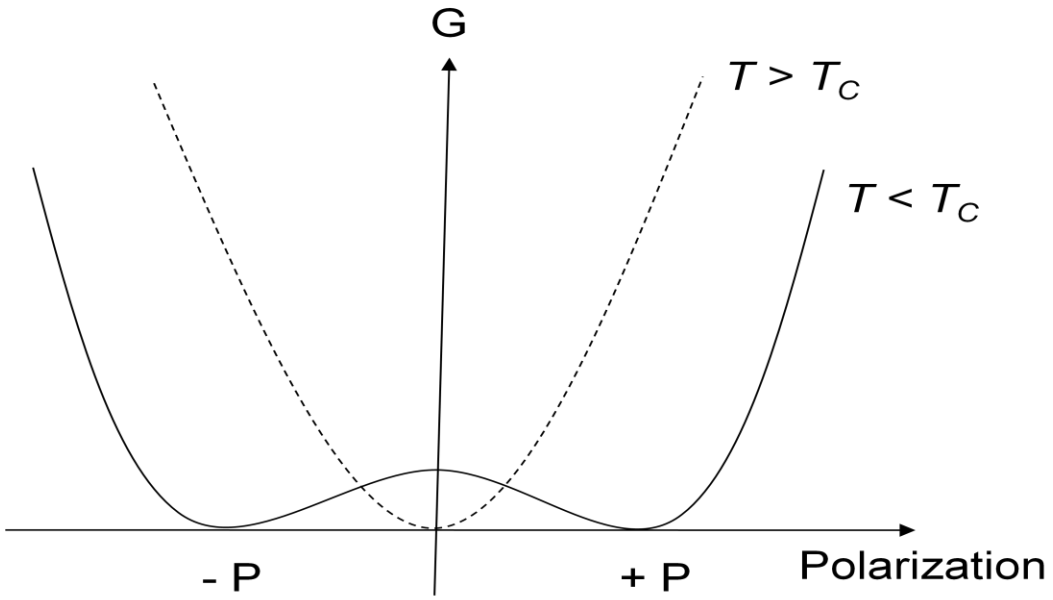

Figure 1.2: Double-well energy diagram, showing free energy (G) vs. polarization at various temperatures. The dashed line and solid line correspond to the possible polarization states in paraelectric and ferroelectric phases, respectively.

The ferroelectrics are characterized by the ferroelectric hysteresis loop. A typical polarization-electric field hysteresis loop displayed by ferroelectrics is shown in Figure 1.3. In the absence of an external electric field, each ferroelectric domain polarizes uniformly, but in different direction, therefore the material appears as non-polar in a macroscopic view. When an electric field is applied to the sample, individual domains are forced to orient along the electric field. Since the electric field is high enough, all the domains align in the same direction and the polarization reaches a saturation value. By decreasing the electric field, the amount of polarization also decreases. When the electric field is completely removed, a major fraction of the domains still keep their alignment,

and therefore a remnant polarization (P_r) is observed. In order to switch the polarization direction, an electric field with opposite direction must be applied. The strength of the electric field required to switch the polarization is called the coercive field (E_C).

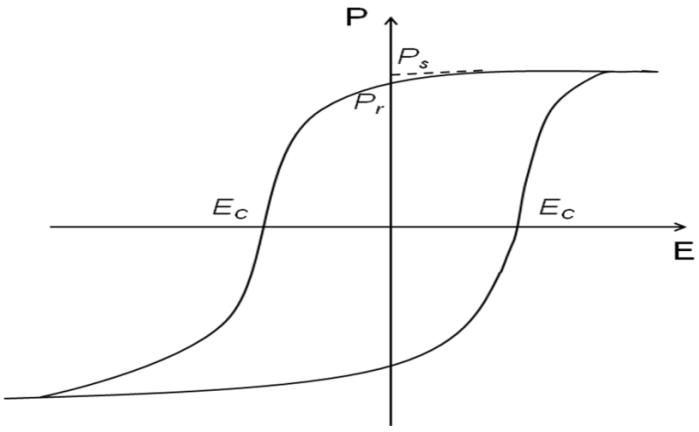

Figure 1.3: A typical ferroelectric polarization-electric field hysteresis loop, showing the direction of spontaneous polarization can be switched by application of an external electric field.

1.3 Ceramic Sintering

In order to be useful, the powder obtained from the solid state reaction step must be pressed into a specific shape and sintered at high temperature to form the ceramics. During the sintering process, a viscous liquid, or sufficient atomic mobility in the solid, is developed to allow its particles to adhere to each other and reduce porosity (i.e, densification). It is known that the surface of a solid has surplus energy due to the fact that the atoms do not have a normal environment, therefore, lowering of the surface

free energy by the elimination of solid-vapor interfaces provides the driving force for sintering [5,6]. In solid-state sintering, the powder does not melt, instead, atomic diffusion occurs when the atoms move from the high energy areas towards the low energy areas by five different sintering mechanisms, as shown in Fig 1.4. These five sintering mechanisms represent the different paths by which the atoms transport from one spot to another [5,6]:

(1) Surface diffusion: Diffusion of atoms along a free surface.

(2) Volume diffusion (from the surface): Atoms of the surface diffuse along the lattice of the solid.

(3) Vapor transport: Atoms evaporate from the surface and condense on a different site.

(4) Grain boundary diffusion: Diffusion of atoms along the grain boundary.

(5) Volume diffusion (from the grain boundary): Atoms from the grain boundary diffuse along the lattice of the solid.

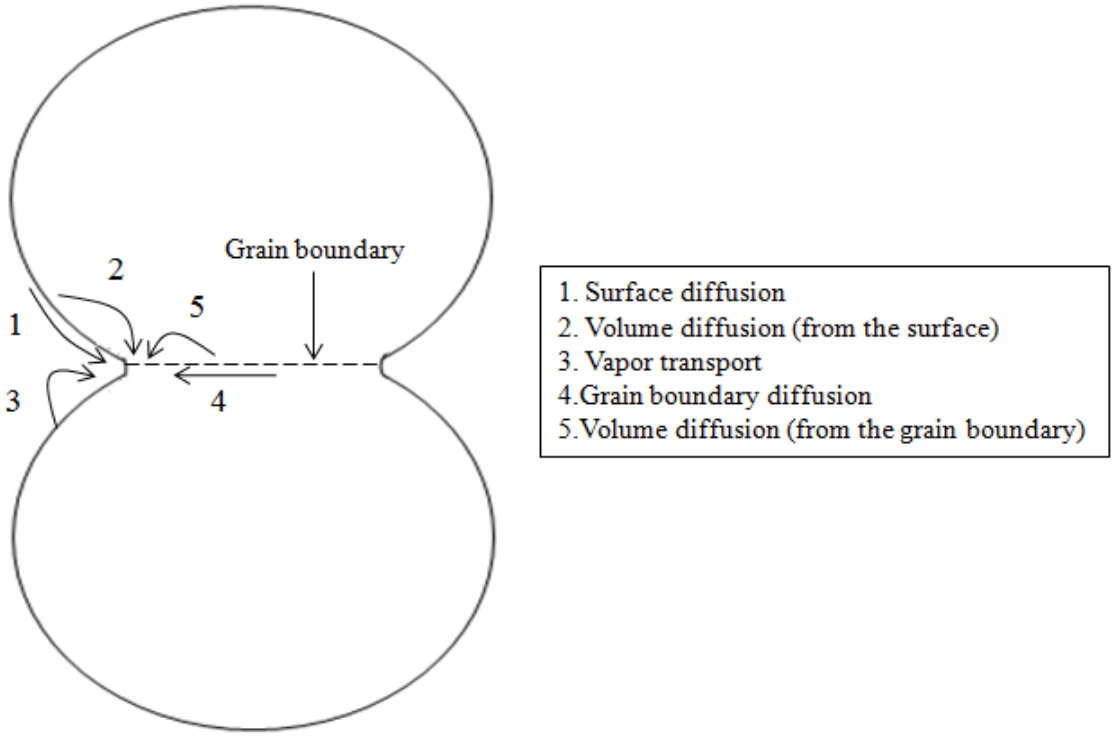

Figure 1.4: Diffusional transport of mater during solid phase sintering.

The properties of ceramics are strongly dependent on the sintering process and mechanism, which in turn is influenced by the starting powder's characteristics and sintering condition. For most of applications, the ceramics with high density (less porosity) are desired. Thus, we shall address some key factors that play important roles in the densification process:

(1) Sintering temperature: Sintering occurs by diffusion of atoms through the microstructure. With increase of temperature, the rate of diffusion is also increased, and

sintering is enhanced. However, if the temperature is too high, the grains can be melted. Therefore, it is important to find the optimal range of sintering temperature.

(2) Sintering duration: Longer sintering duration allows the atoms moving in longer distance in the particles, which facilitate the densification process. In general, the influence of duration time on sintering is less than the influence of the sintering temperature.

(3) Pressure: In most cases, ceramics are sintered by pressureless sintering. However, pressure sintering or “hot pressing” can assist densification in some difficult cases. In this technique, an external pressure is applied during the heating treatment [5]. Pressure sintering is a complex and expensive technique because it requires a pressure device that withstands the high sintering temperature. Nevertheless, it can significantly enhance the densification rate, which means a lower sintering temperature and a shorter sintering time can be used in hot pressing than in pressureless sintering. Hot pressing is commonly used in the systems that contain volatile components or if they decompose at a higher temperature.

(4) Sintering atmosphere: The sintering atmosphere has several important effects on the chemical composition of the ceramics. For example, evaporation of volatile PbO can occur during sintering, making the chemical composition varied in lead-based

electroceramics [7,8]. A common solution is to surround the sample pellets with pre-calcined powder having the same composition as the sample. For other systems, such as silver niobate, an oxygen atmosphere is required in sintering to prevent Ag_2O from being reduced to metallic silver [9].

(5) Impurity: The impurities in solid solution are usually located close to the surface of particles or at grain boundaries. The interaction of the impurities and nearby molecules can influence the atomic diffusion rate in sintering.

(6) Particle size: The rate of shrinkage is closely related to the particle size. Smaller powder particles have a larger surface to volume ratio, which enhances the movement of atoms from the bulk into the surface of the pores thereby reducing porosity [5,6].

1.4 Perovskite ABO_3 Structure

Since the discovery of the first ferroelectric perovskite, $BaTiO_3$, in the early 1940's, a large series of new ferroelectric materials have been developed. Among these materials, the perovskite family of the general formula ABO_3 is considered to be the most important ferroelectric prototype. The simple cubic structure (point symmetry m3m) is made up of an array of corner sharing BO_6 octahedra with the A cation occupying the

twelve-coordinated cavities. The crystal structure of the perovskite structure is illustrated in Figure 1.5. Stoichiometric ABO_3 perovskites have the sum of A and B oxidation numbers equal to 6, therefore there are three combinations of valence for the A and B cations: $A^{I}B^{V}O_3$ (A = Na, Ag, K; B = Nb, Ta), $A^{II}B^{IV}O_3$ (A = Ba, Sr, Ca, Pb; B = Ti, Sn, Zr, Hf, Mn, Mo, Fe, Ce, Pr, U), $A^{III}B^{III}O_3$ (A = Ln, Bi, Y; B = Fe, Cr, Co, Mn, Ti, V, Al, Sc, Ga, In, Rh) [10]. Many of the first two series exhibit ferroelectric properties caused by a small distortion of the cubic unit cell.

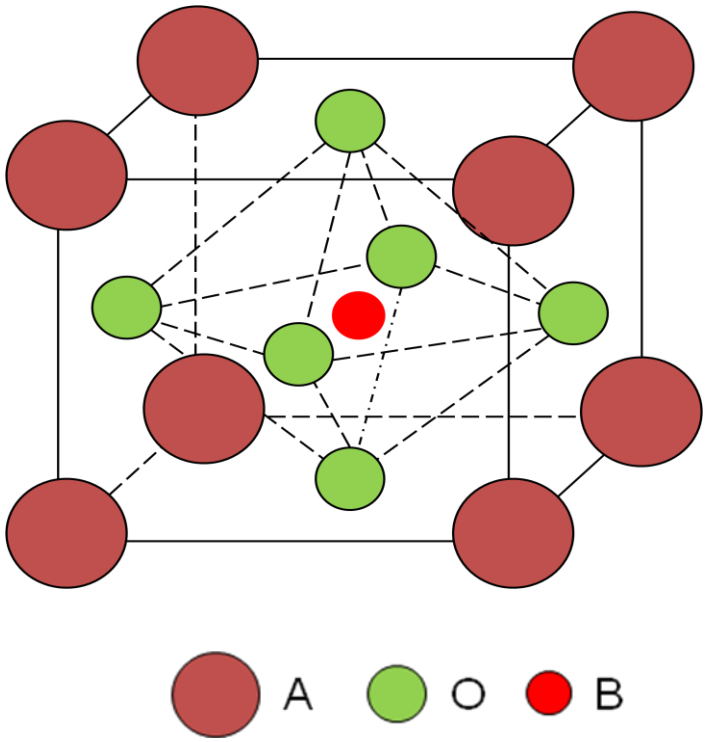

Figure 1.5: Cubic unit cell of Perovskite structure ABO_3.

$BaTiO_3$ is still one of most used ferroelectric materials so far. The high polarizability of $BaTiO_3$ makes it a useful material for ceramic capacitor applications. Upon cooling, $BaTiO_3$ undergoes a phase transition from a paraelectric to a ferroelectric phase at the Curie temperature T_C =120 ^oC. At temperatures above T_C, the unit cell is cubic and the Ti^{4+} ion is in the center of the oxygen octahedron, giving rise to centro-symmetric non-polar structure, as shown in Fig 1.5. On cooling below T_c, the unit cell is distorted to become tetragonal. The Ti^{4+} ion is no longer in the center, instead, it shifts to occupy an off-center position. This off-center displacement of the Ti^{4+} ion in the perovskite structure is stabilized by the Ti-3d and O-2p hybridization in $BaTiO_3$. The displacement of Ti^{4+} ion results in a spontaneous polarization, the direction of which is along one of the 6 <001> directions in the tetragonal phase. Further decrease of temperature changes the crystal structure to orthorhombic (O) at 5^oC and rhombohedral (R) phases at -90^oC. $PbTiO_3$ is another well known perovskite compound, which has a Curie temperature of 490^oC [11] at which point the cubic unit cell is transformed into a tetragonal structure. The presence of lone pair $6s^2$ electrons of Pb^{2+} causes the off-center displacement of the A-site cation, which further increases the tetragonality of the perovskite structure and gives a large polarization, thus enhancing the ferroelectric state.

1.5 Lead-Free Ferroelectric Materials

Lead-based ferroelectric materials, such as $Pb(Zr,Ti)O_3$ (PZT) and $Pb(Mg_{1/3}Nb_{2/3})O_3$-$PbTiO_3$ (PMN-PT), have been used in a wide variety of electronic device applications, i.e., piezoelectric transducers, sensors, actuators and non-volatile memory, because of their exceptional piezoelectric and ferroelectric properties [1, 12]. However, because illegally-dumped lead-containing devices may release toxicity and cause serious health and environmental hazards, the Pb-based materials are currently facing global restrictions. Therefore, there are interest and need on development of piezo-/ferroelectric materials that are less toxic and more nvironmentally friendlier recently.

1.5.1 $KNbO_3$-Based Systems

Potassium niobate $KNbO_3$ (KN) exhibits a similar sequences of phase transitions as $BaTiO_3$, transforming from cubic → tetragonal → orthorhombic → rhombohedral at 425^{o}C, 225^{o}C, and -10^{o}C, respectively. $KNbO_3$ has received considerable interest as a candidate for lead-free materials in piezoelectric applications, since it has a high T_C (425^{o}C) [13] and demonstrates an excellent electromechanical coupling factor when in the form of a single crystal [14,15]. Compared with single crystal growth, preparation of

sintered ceramics is an easier and less expensive process from the commercial point of view. However, because of the poor sinterability of $KNbO_3$ ceramics by conventional sintering processes, there are only a limited number of reports available on the electric properties of KN ceramics. The densification of KN ceramics is difficult because potassium oxide (K_2O) becomes volatile at temperatures over 800^oC during sintering. Its evaporation from the system causes the ratio of K/Nb differs from unity. As a result, some unwanted secondary phases form in the final product [16, 17]. Recently, some research groups reported that additions of small amounts of elements, such as La, Fe, Mn, Co, and Pb, resulted in dense KN ceramics by ordinary sintering [16-19]. Moreover, both the ferroelectric and piezoelectric properties of the sintered ceramics were enhanced significantly.

1.5.2 $(K_{0.5}Na_{0.5})NbO_3$-Based Systems

$KNbO_3$ and $NaNbO_3$ form a solid solution across the whole compositional range. (1-*x*)$KNbO_3$ - *x*$NaNbO_3$ ceramics at a composition of $x = 0.50$ ($K_{0.5}Na_{0.5}NbO_3$, KNN) exhibit a high T_C at 420^oC [20] and good piezoelectric properties, such as a large planar coupling factor, $k_p = 0.56$, and a large piezoelectric coefficient, d_{33} up to 160 pC/N [21, 22]. Therefore, KNN is considered as another promising candidate for lead-free

piezoelectric materials. $(K_{0.5}Na_{0.5})NbO_3$ has been widely believed to be the optimum composition for the piezoelectric response in the KNN-based ceramics, because there is a morphotropic phase boundary (MPB) near the 50/50 composition separating two different orthorhombic phases (Figure 1.6). Within the MPB region, the coexisting phases facilitate polarization rotation during the poling process, since the number of possible polarization directions is increased compared to a single phase [23]. The MPB has also been identified in some other solid-solution systems, such as $(1-x)Pb(Mg_{1/3}Nb_{2/3})O_3$-$xPbTiO_3$ [24-26], and $Pb(Zr_{1-x}Ti_x)O_3$ [27]. They all exhibit a maximum piezoelectric performance in the MPB region.

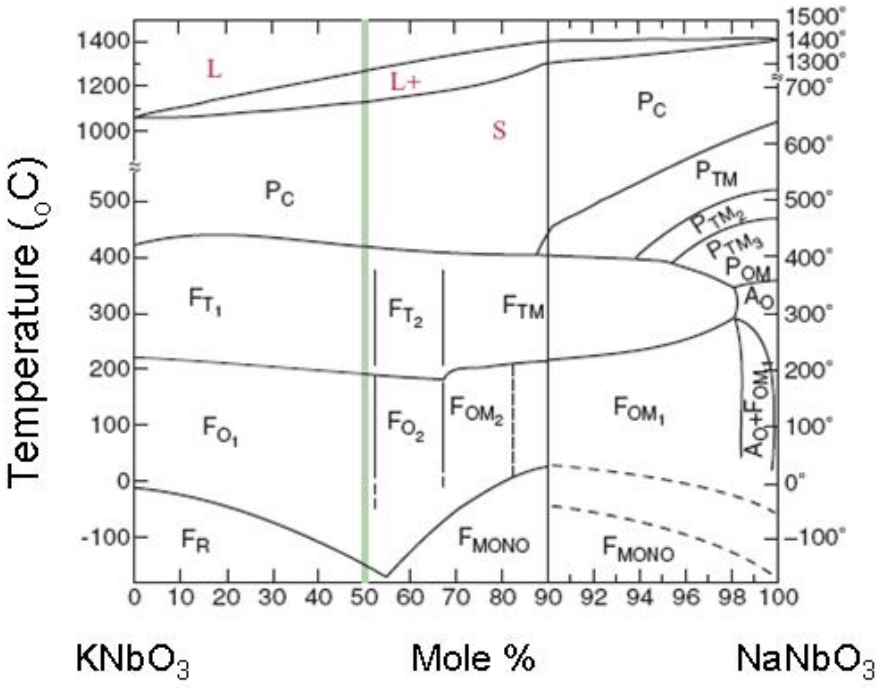

Figure 1.6: Binary phase diagram of $KNbO_3$-$NaNbO_3$ solid solution (adapted from Ref, [28]).

Similar to KN ceramics, the synthesis of high density KNN ceramics has been difficult by conventional sintering. Recently, it was reported from our group that KNN ceramics with relative high density could be prepared by using potassium fluoride (KF) as a sintering agent [29]. Furthermore, solid solutions between KNN and other ferroelectric compounds, including KNN-$LiNbO_3$ [30], KNN-$BaTiO_3$ [31], KNN-$Bi_{0.5}Na_{0.5}TiO_3$ [32], KNN-$AgNbO_3$ [33], etc, were studied to improve piezoelectric properties.

1.5.3 $AgNbO_3$-Based System.

Silver niobate ($AgNbO_3$, AN) has attracted much attention in recent years due to its interesting chemical and physical properties. AN undergoes a phase transition from a paraelectric to weak ferroelectric phase at a high Curie temperature (T_C = 360 ^oC) [34]. It is well known that the ferroelectricity of this material is very weak at room temperature due to the tilting of oxygen octahedral of perovskite with a small A-site ion, i.e, Ag^+ (see Fig 4.10). Grinberg and Rappe used density functional theory (DFT) calculations to predict that a strong ferroelectricity of AN can be induced by alloying AN with other ferroelectric materials, such as $BaTiO_3$ and $PbTiO_3$ [35]. Later, Fu *et al* discovered that an extremely large polarization (52 $\mu C/cm^2$) was induced in AN ceramics when a large

external electric field was applied [36]. These findings provide theoretical guide lines to improve the ferroelectric properties of $AgNbO_3$ for the application as lead-free electromechanical transducer materials.

1.6 Objectives of This Study

As mentioned earlier, there is an increasingly strong demand to develop lead-free piezoelectrics that can compete with the Pb-based materials. Figure 1.7 shows the number of publications on some of "hot" lead-free piezoelectrics for the time period from 2000 to 2009. The increasing numbers of publications on lead-free piezoelectric materials reflects this fast developing area of research. It can be seen that the alkali-niobate-based systems, including $KNbO_3$ and $K_{0.5}Na_{0.5}NbO_3$, contribute the two of most studied families of lead-free materials in the last few years. However, so far non-Pb piezoelectric ceramics usually have weaker piezoelectricity (d_{33} < 150 pC/N in most of lead-free systems) compared with PMN-PT and PZT. Although some KNN-based textured ceramics, such as $(K_{0.44}Na_{0.52}Li_{0.04})(Nb_{0.84}Ta_{0.10}Sb_{0.06})O_3$, have shown an increased d_{33} of 416 pC/N [37], its expensive and complicated synthetic routes limit the actual applications. Therefore, it is of interest to search for new lead-free materials in order to achieve high ferroelectric and piezoelectric performances.

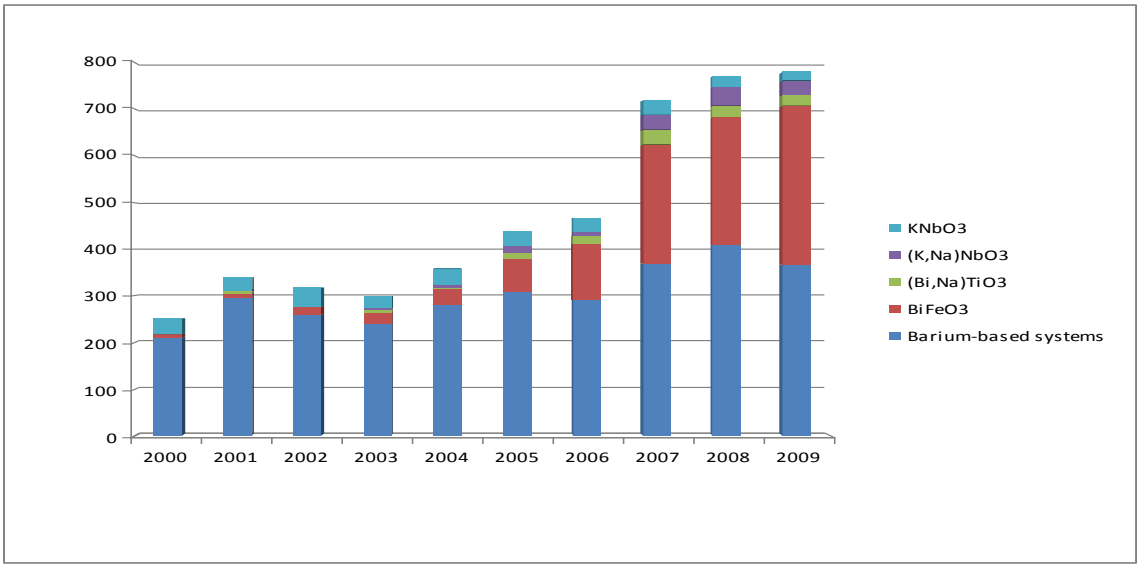

Figure 1.7: Number of publications on some selected lead-free piezoelectrics for the time period from 2000 to 2009. The statistics was carried out by counting the relevant papers in "ISI Web of Science". Note that Barium-based systems include $BaTiO_3$ and $Ba(Zr,Ti)O_3$.

In this thesis work, we synthesized the $AgNbO_3$-based solid solutions with the substitution of $KNbO_3$ and $K_{0.5}Na_{0.5}NbO_3$, and characterized their structure and physical properties. Both KN and KNN are normal ferroelectrics with larger A-site ions than in AN. It is hypothesized that the A-site substitution by K^+ and K^+/Na^+ ions would change the crystal structure of $AgNbO_3$ and induce a normal ferroelectric state from the weak ferroelectric AN, thereby enhancing the dielectric, and piezoelectric properties.

The first part of our work (**Chapter 3**) is on the synthesis of the $(1-x)AgNbO_3$-$xKNbO_3$ solid solution in the form of ceramics by a solid state reaction, and characterization of its structural, dielectric, and ferroelectric properties by means of X-ray diffraction, dielectric spectroscopy, and ferroelectric hysteresis loop measurement.

Note that, during this investigation, we became aware of a report on a similar system published by Fu *et al* in Nov, 2009 [38]. However, the results presented in Chapter 3 are from our independent and original work, which had been performed before the report of Fu *et al*.

Chapter 4 reports the preparation of a new solid solution of (1-*x*)$AgNbO_3$-*x* $K_{0.5}Na_{0.5}NbO_3$ in the form of ceramics, and the characterization of the structural, dielectric, ferroelectric, piezoelectric properties. In particular, the crystal structural analysis of this system was carried out to confirm the composition-induced phase transition from a centro-symmetric phase in AN to a non-centrosymmetric polar ferroelectric phase. This provides a better understanding of structure-property relationships in $AgNbO_3$-based materials.

Lastly, **Chapter 5** gives general conclusions and provides some possible future directions for the further studies of the $AgNbO_3$-based piezo-/ferroelectric materials.

References

[1] G.H. Haertling, J. Am. Ceram. Soc., **82**, 797 (1999).

[2] J. F. Nye, *Physical Properties of Crystals*, Clarendon Press, Oxford (1964).

[3] http://www.bostonpiezooptics.com/files/Intro_to_Piezo.pdf

[4] M.E. Lines, and A. M. Glass, *Principles and Applications of Ferroelectrics and Related Materials*, Clarendon Press, Oxford (1977).

[5] M. N. Rahaman, *Sintering of Ceramics*, CRC Press (2008).

[6] P. Boch, and J-C. Niepce, *Ceramic Materials Processes, Properties and Applications*, ISTE Ltd (2007).

[7] D. A. Northrop, J. Am. Ceram. Soc., **50**, 441 (1967).

[8] D. A. Northrop, J. Am. Ceram. Soc., **51**, 357 (1968).

[9] M. Lukaszeski, Phase Transition **3**, 247 (1983).

[10] *C.N.R Rao , and B.Raveau. Transition Metal Oxides, Second Edition, John Wiley & Sons, Ltd (1998).*

[11] B. Jaffe, W.R. Cook, Jr., and H. Jaffe, *Piezoelectric Ceramics*,Academic Press, London (1971).

[12] L. E. Cross, *Ferroelectrics **76**, 241 (1987).*

[13] G. Shirane, R. Newnham and R. Pepinsky G. Shirane , Phys. Rev. **96**, 581(1954).

[14] K. Nakamura, T. Tokiwa, and Y. Kawamura, J. Appl. Phys. **91**, 9272 (2002).

[15] S. Wada, A. Seike, and T. Tsurumi, Jpn. J. Appl. Phys. **40**, 5690 (2001).

[16] T. Wada, A. Suzuki, and T. Saito, Jpn. J. Appl. Phys. **45**, 7431 (2006).

[17] S. Tashiro, H. Nagamatsu and K. Nagata, Jpn. J. Appl. Phys. **41,** 7113 (2002).

[18] K. Kakimoto, I. Masuda and H. Ohsato, Jpn. J. Appl. Phys. **43,** 6706 (2004).

[19] K. Matsumoto, Y. Hiruma, H. Nagata and T. Takenaka., Jpn. J. Appl. Phys. **45**, 4479(2006).

[20] R. E. Jaeger, L. Egerton J Am Ceram Soc **45**,209 (1962).

[21] L. Egerton, and D. M. Dillon, J. Am. Ceram. Soc. **42**, 438 (1959).

[22] G. H. Haertling, J. Am. Ceram. Soc., **50**, 329 (1967).

[23] W.Cao, and L. E. Cross, Phys. Rev. B **47**, 4825 (1993).

[24] S. E. Park, and T. R. Shrout, J. Appl. Phys. **82**, 1804 (1997).

[25] Z.-G. Ye, *B.* Noheda, M. Dong, D. Cox, and G. Shirane, Phys. Rev. B **64,** 184114 (2001).

[26] B. Noheda, D.E. Cox, G. Shirane, J. Gao and Z.G. Ye, Phys. Rev. B **66,** 054104 (2002).

[27] B. Noheda, D.E. Cox, G. Shirane, J.A. Gonzalo, L.E. Cross, and S.E. Park, Appl. Phys. Lett., **74,** 2059 (1999).

[28] A. Safari, and E. K. Akdogan, *Piezoelectric and Acoustic Materials for Transducer Applications*, Springer, USA, (2008).

[29] A. Gronotte, *Development of New Chemical Processes to Lead-Free Piezo- and Ferroelectric Materials* (Simon Fraser University, 2006)

[30] YP Guo, K. Kakimoto and H. Ohsato, Appl. Phys. Lett. **85**, 4121 (2004)

[31] Y. Guo, K. Kakimoto, and H. Ohsato, Jpn. J. Appl. Phys. **43**, 6662 (2004).

[32] R. Zuo, X. S. Fang, and C. Ye, Appl. Phys. Lett. **90**, 092904 (2007).

[33] C. Lei, and Z-G. Ye, Appl. Phys. Lett. **93**, 042901 (2008).

[34] A. Kania, J. Phys. D. **34,** 1447 (2001).

[35] I. Grinberg and A. M. Rappe, App. Phys. Lett. **85,** 1760 (2004).

[36] D. S. Fu, M. Endo, H. Taniguchi, T. Taniyama, and M. Itoh, Appl. Phys. Lett. **90,** 3 (2007).

[37] Y. Saito, H. Takao, T. Tani, T. Nonoyama, K. Takatori, T. Homma, T. Nagaya, and M. Nakamura, Nature (London) 4**32**, 84 (2004).

[38] D. Fu, M. Itoh, and S. Kashihara, J. Appl. Phys. **106**, 104104 (2009).

Chapter 2

Measurements and Characterization:

Principles and Techniques

2.1 Introduction

In this chapter, a brief introduction to the principles and concepts of various characterization techniques used in this thesis work is described. These characterization techniques include X-ray diffraction (XRD) for structural analysis, impedance spectroscopy for dielectric properties studies, ferroelectric hysteresis loop measurement, and piezoelectric measurement.

2.2 Powder X-Ray Diffraction (XRD)

2.2.1 Principle of X-ray diffraction

X-ray diffraction has been extensively used as a “fingerprint” for the identification of crystalline materials, since different materials do not have the same powder diffraction patterns due to the difference in structural type, unit cell size, and atomic number.

X-rays are an electromagnetic radiation with the wavelength in the range of 0.1 to 100 Å, which is found between the gamma and ultraviolet radiation in the electromagnetic spectrum. To generate X-rays, a beam of electrons is accelerated by a high electric field (larger than 30 kV) and directly bombards a metal target, e.g., a piece of copper [1]. The high speed electrons hit the target causing 1s electrons of the metal to be knocked out from their energy shells (*K* shell). When a higher energy level electron from either 2p or 3p orbital drops down and fills the vacancies in K shell, a characteristic X-ray is emitted. Generally speaking, X-rays produced by electrons falling back from the *L* to the *K* shell (2p-1s transition) is designated K_α, whereas the electrons falling back from the *M* to the *K* shell (3p-1s transition) is designated K_β [2]. For a copper target, the $K\alpha$ radiation (λ=1.5148 Å) is usually selected as a monochromatic beam for the source of the powder X-ray diffraction because of its comparably higher intensity. The K_β radiation (λ=1.3926 Å) can be filtered out by a nickel foil filter effectively.

In the diffraction method, a monochromatic beam of X-rays strikes the sample and the reflection of X-rays generated from the planes in the crystal lattices of the samples give rise to the distinct diffraction pattern. The principle of Bragg diffraction from a set of planes in a crystal lattice is illustrated in Figure 2.1. The incident rays hit the crystal planes with an incident angle θ, and diffract at the Bragg angle θ. The diffraction

peak is observed if the conditions satisfy the Bragg's law [2]:

$$2d_{hkl}sin\theta = n\lambda \quad , \qquad (2.1)$$

where d_{hkl} is the spacing between the crystal planes, θ is the angle between the incident beam and the planes, n is an integer number, and λ is the wavelength of incident beam.

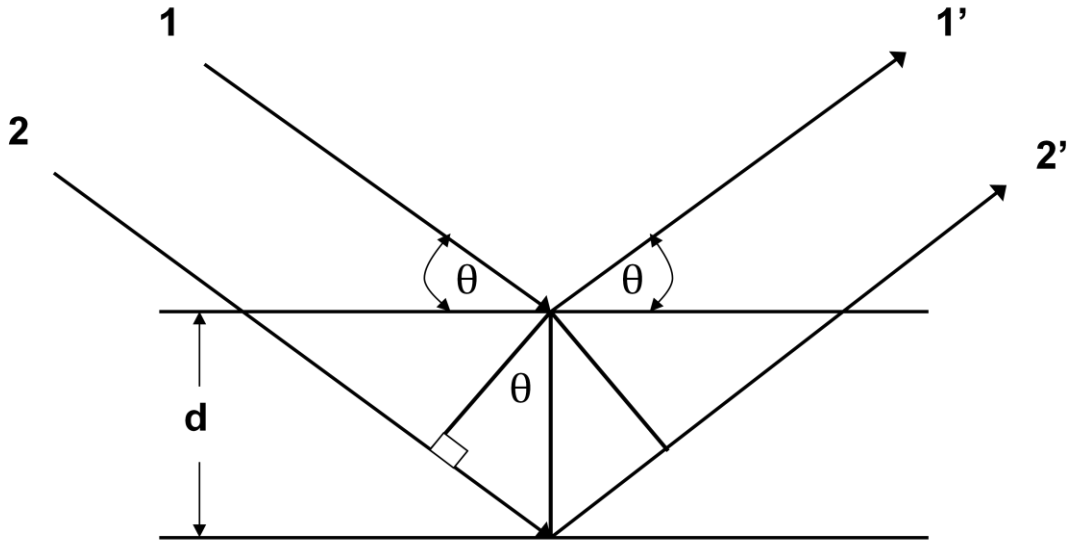

Figure 2.1: Diffraction principle and deviation of Bragg's law. It shows that the incident x-ray hits a set of crystal planes (with interplanar spacing of d_{hkl}) at an angle of θ and reflects at that same angle from the planes.

2.2.2 Crystal Structure Characterization

The X-ray diffraction patterns, which are plots of the intensity of the Bragg's peaks as a function of 2θ, are used to determine the crystal structure and to monitor the purity of phases after chemical reactions. It is almost impossible to find two different

substances that have exactly the same XRD pattern. Even for the compounds with the same structural types, the difference in symmetry and unit cell parameters give rise different peak positions. The intensities of the peaks are related to the X-ray scattering power of the atoms in the compound. The presence of different types of ions with different atomic numbers also varies the peak intensity. In a polycrystalline sample, each small crystal is built up of regular orientation of atoms with repeatable unit cells. A unit cell is characterized by six parameters, three axial lengths of the unit cell edges (*a*, *b*, and *c*) and three interaxial angles (α, β, and γ), as shown in Figure 2.2. The *d*-spacing, d_{hkl}, is directly related to these lattice parameters. Their relationship is described by various equations for different unit cell types. For example, the crystal systems with orthogonal axes, i.e. cubic, tetragonal, and orthorhombic, exhibit the equations as follows [2]:

$$\frac{1}{d_{hkl}^2} = \frac{h^2}{a^2} + \frac{k^2}{b^2} + \frac{l^2}{c^2} \quad , \tag{2.2}$$

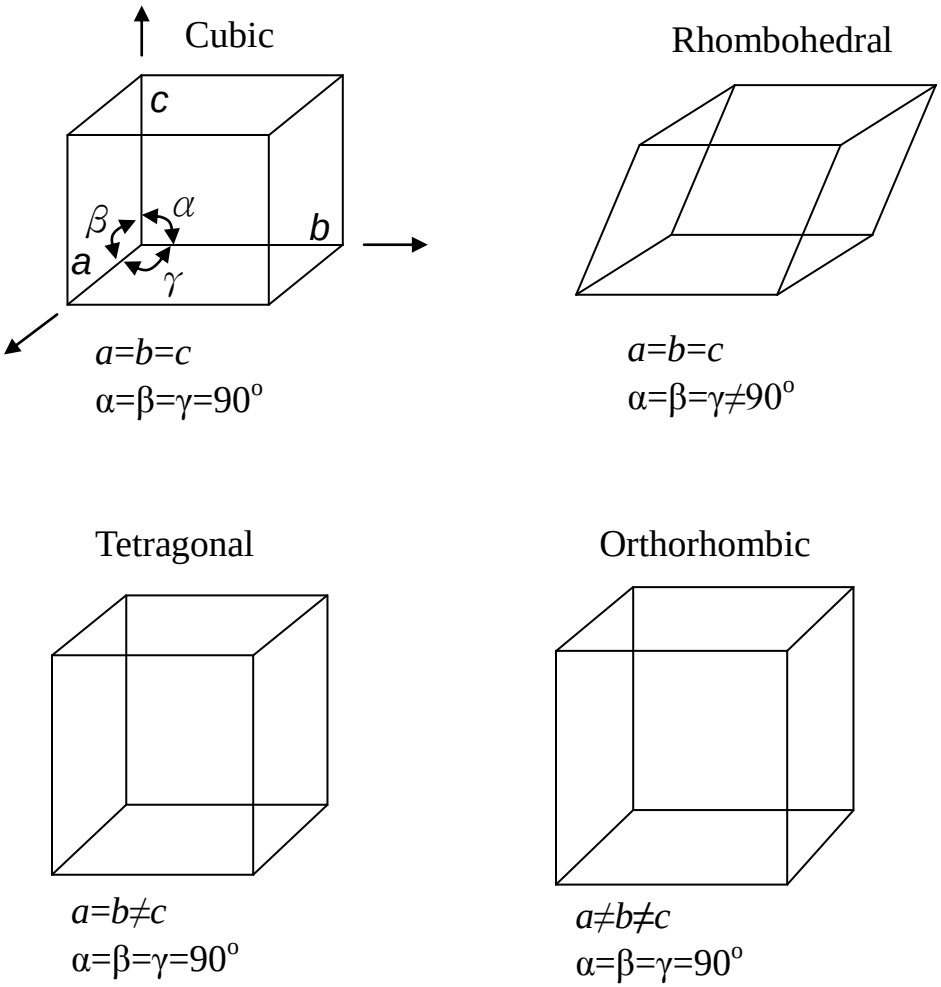

Figure 2.2: Illustration of the lattices of primitive cubic, rhombohedral, tetragonal, and orthogonal unit cells with corresponding lattice parameters.

When a crystal undergoes a structural phase transition, because of the change in lattice parameters, the X-ray diffraction pattern also changes. For example, in the cubic phase, the length of the unit cell edges are equal ($a = b = c$), and the three interaxial angles are all the same ($\alpha = \beta = \gamma = 90^{o}$C). As a result, the *d*-spacing of the equivalent

(001), (010), and (100) planes are the same, therefore, a single peak is shown for the {100} series of planes. As the unit cell changes from cubic to tetragonal phase, the interaxial angles are kept the same ($\alpha = \beta = \gamma = 90^{o}$C), however, the lengths of the unit cell are no longer all equal ($a = b \neq c$). The {100} diffraction peak in tetragonal phase will split into two peaks, i.e. the (100)/(010) and (001) peaks. This is because the lattice parameters *a* and *b* are equal ($\alpha = \beta$) and are different from *c*. Figure 2.3 shows the corresponding splitting of {111}, {200}, and {220} reflections as the crystal structure change from cubic to the lower symmetry phases.

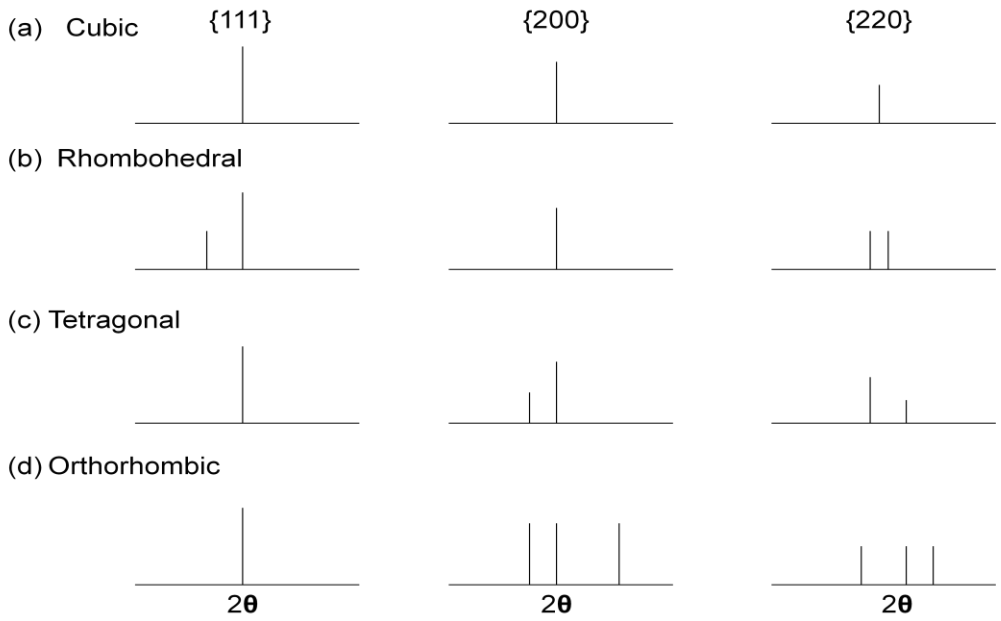

Figure 2.3: Characteristic X-ray diffraction patterns of {111}, {200}, and {220} crystallographic planes for the Cubic, Rhombohedral, Tetragonal, and Orthorhombic symmetries, showing their corresponding peak splitting.

2.3 Measurements of Dielectric Permittivity

To investigate the dielectric properties of the ferroelectric materials, the dielectric permittivity as a function of temperature at different frequencies is measured by means of either an Alpha high resolution dielectric/impedance analyzer (NovoControl) or a Solartron 1260 impedance analyzer associated with a Solartron 1296 dielectric interface. Figure 2.4 shows a schematic of the circuit in a real electric permittivity measurement. When an alternating voltage with a small amplitude (usually |V| < 3V) is applied on a sample capacitor (C_s) and a reference capacitor (C_r), the voltage (V_r) across the reference capacitor is measured. Since the sample capacitor and the reference capacitor are connected in series, the charge developed on the two capacitors must be the same, that is, $Q_r = Q_s$. So the charge on the sample can be calculated by:

$$Q = C_r \times V_r \quad . \qquad (2.3)$$

The voltage (V_s) is also measured across the sample, therefore the capacitance of the sample can be found by:

$$C_s = Q / V_s \quad . \qquad (2.4)$$

Once the capacitance of the sample (C_s) is obtained, the dielectric permittivity can be determined by the following equation:

$$C = \varepsilon_r \varepsilon_o (A/d) \quad , \qquad (2.5)$$

where ε_o is the permittivity of free space, 8.854×10^{-12} F/m, ε_r is a relative permittivity, A is the area of plates of the parallel electrodes, and d is the thickness between the electrodes [3, 4].

It is known that all dielectric materials exhibit two types of dielectric losses. One is a conduction loss, which comes from the flow of actual charges through the dielectric. The other is a dielectric loss due to the movement of atoms or molecules in an alternating electric field. Because the dielectric loss is frequency dependent, the dielectric permittivity has to be written in a complex form:

$$\varepsilon_r(f) = \varepsilon'(f) - i\,\varepsilon''(f) \quad , \qquad (2.6)$$

where ε' is the real part of the dielectric permittivity (commonly called the dielectric constant), $i = \sqrt{-1}$, and ε'' is the imaginary part of the dielectric permittivity. The latter ε'' is related to the dielectric loss. But the tangent of the dielectric loss angle, tan δ, is more frequently used to describe the energy loss in dielectric materials [5]. The dielectric loss tangent is defined as:

$$\tan\delta = \varepsilon'' / \varepsilon' \quad , \qquad (2.7)$$

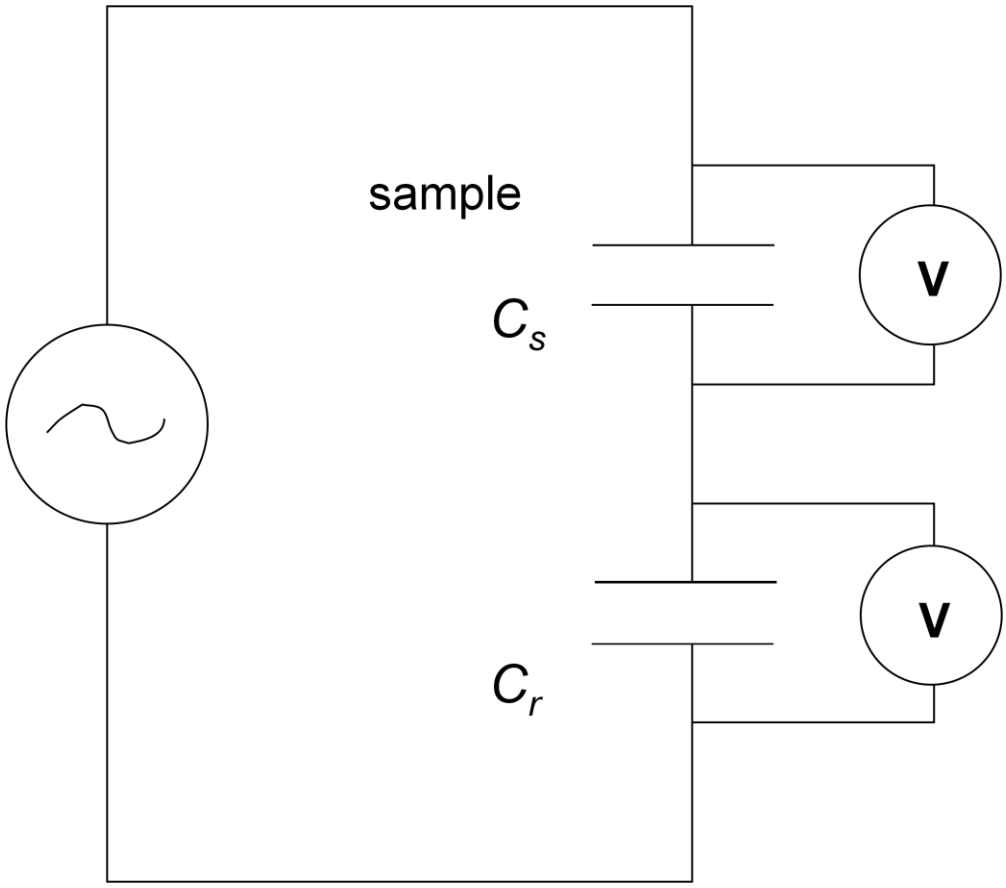

Figure 2.4: Principle of a dielectric permittivity measurement (adapted from Ref. [6]).

2.4 Ferroelectric Measurement

In this work, the ferroelectric measurements were carried out to display the polarization-electric field hysteresis loop, using an RT66A Standard Ferroelectric Testing System (Radiant Technologies Inc.) combined with an RT66A high voltage interface

(HVI) [7]. In a ferroelectric hysteresis loop measurement, the opposite surfaces of the ceramic samples are coated with a layer of silver paste to make the electrodes. Gold wires are then used to connect the surface electrodes of the sample to the electrical circuit. The electric polarization as a function of electric field is measured based on the principle of Sawyer-Tower circuit [8], as shown in Figure 2.5. An amplified A.C. voltage is cycled by the signal generator, and applied on the sample and reference capacitor. The resulting charge, Q, of the reference capacitor is determined by the equation:

$$Q = C_R V_R \quad . \qquad (2.8)$$

Since the charge on the reference capacitor is the same as the charge on the ferroelectric sample by the fact that they are in series, the polarization, P, of the sample can be obtained directly as follows:

$$P = Q/A \quad , \qquad (2.9)$$

where A is the electrode area of the sample. Using a software, it is then possible to plot the polarization against the ac electric field applied across the sample, displaying a hysteresis loop for a ferroelectric material.

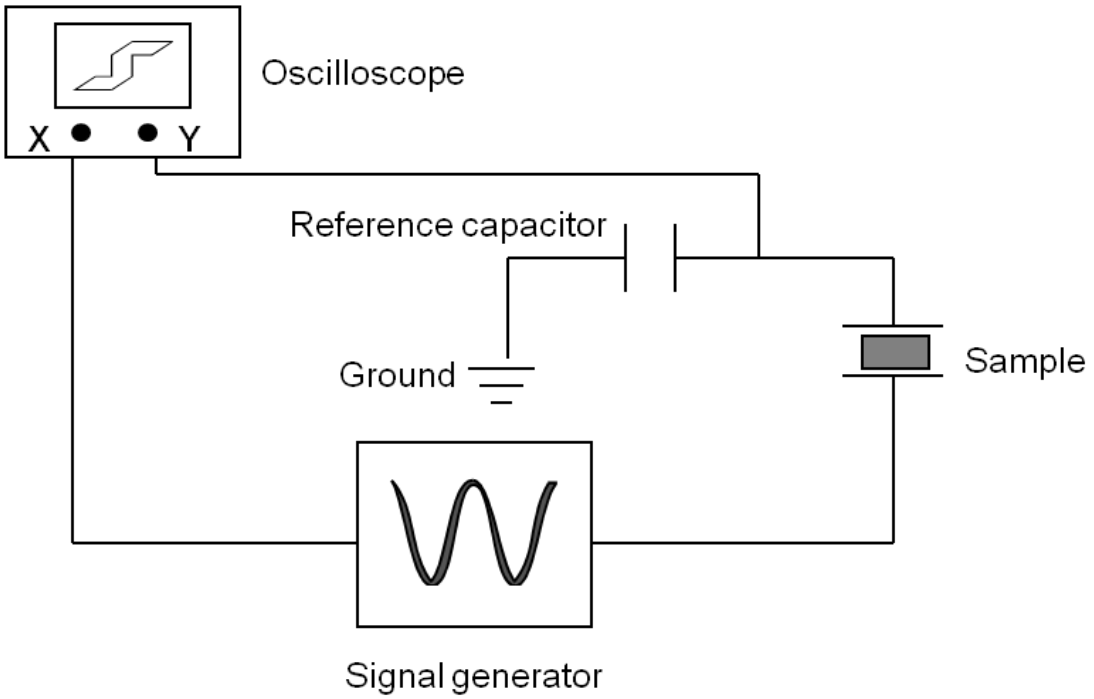

Figure 2.5: A modified Sawyer-Tower circuit for the measurement of ferroelectric hysteresis loops (Adapted from Ref. [9]).

It is known that a ferroelectric hysteresis loop obtained from measurement has contributions from three parts: (1) the dielectric contribution, which is linear response of the polarization to the applied electric field without hysteresis behaviour [Figure 2-6 (a)]; (2) the domain switch contribution, which shows a rectangle hysteresis loop where the polarization is reversible with the external electric field applied in opposite direction [Figure 2-6 (b)]; (3) the leakage current contribution, which display the shape of an ellipse in response of the electric field [Figure 2-6 (c)]. The electric polarization arising from the leakage current can be described by the following equation:

P = (Current x time)/Area . (2.10)

It is clear that the leakage current contribution is time and frequency dependent. The low frequency may cause a larger leakage current contribution. Therefore, the sample measured in various frequencies shows different hysteresis loops. The measurement is usually done at high frequency to obtain the information of true polarization from the domain switching.

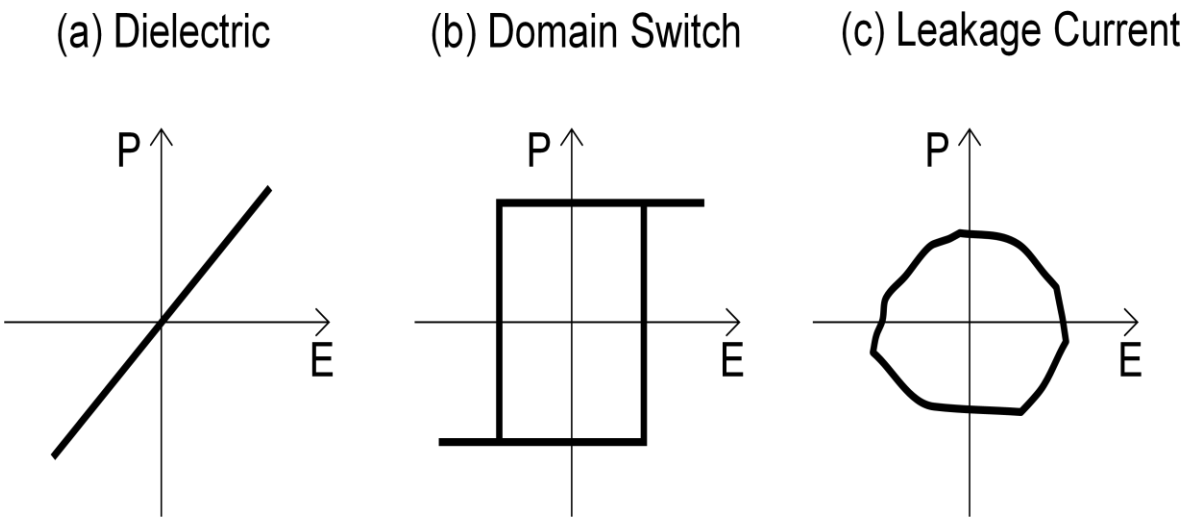

Figure 2.6: Three components of an electric hysteresis loop.

2.5 Determination of Piezoelectric Constants

The piezoelectric properties of the materials studied in this work were characterized using a Piezo-d_{33}/d_{31} Meter (ZJ-6B, China). This quasi-static testing method is one of most commonly used technique for the measurement of piezoelectric

coefficients. The schematic setup for the d_{33} measurement is shown in Figure 2.7. A piezoelectric sample between the top and bottom metallic probes is subjected to a quasi-static force (about 0.25 Newton with a frequency of about 110 Hz) and the electric charge on the electrodes is analyzed. The piezoelectric coefficient d_{33} can be defined by the following equation:

$$d_{33} = \left[\frac{D_3}{T_3}\right], \tag{2.11}$$

where D_3 is the electric displacement in Z-direction, and T_3 is mechanical stress also applied in Z-direction.

This expression of d_{33} can be rewritten as follows:

$$d_{33} = \frac{Q/A}{F/A} = \frac{Q}{F} = \frac{C \times V}{F}, \tag{2.12}$$

where A is area stressed by the force F, C the capacitance in the circuit , V the voltage generated across the capacitor. The d_{33} coefficient of a sample can be determined by measuring the piezoelectric charge across the tested sample for a given force, the charge developed from the sample is then compared with built-in reference, which enables the system to give a direct reading of d_{33} in pC/N.

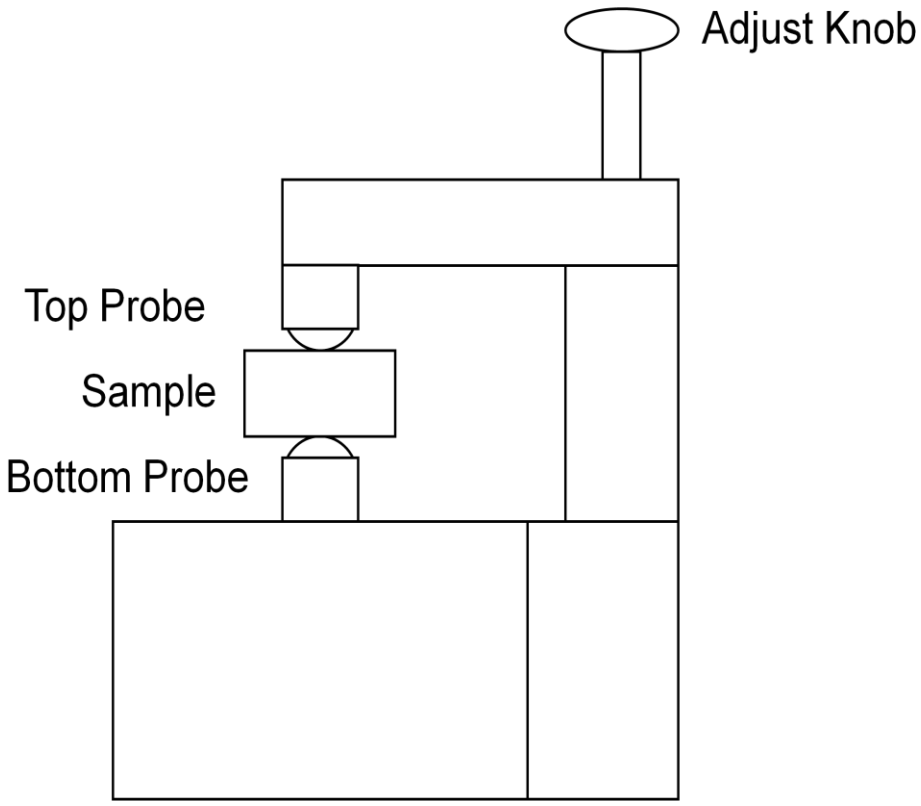

Figure 2.7: A schematic diagram for the d_{33} testing experiment (adapted from Ref.[10]).

References

[1] M. Ladd and R. Palmer, *Structure Determination by X-ray Crystallography* (Kluwer Academic/Plenum Publishers, New York, 2003).

[2] L. E. Smart and E. A. Moore, *Solid State Chemistry* (Taylor & Francis, London, 2005).

[3] A.R. West, *Basic Solid State Chemistry (*John Wiley & Sons, New York, 1999).

[4] E.Barsoukov and J. R. Macdonald, *Impedance Spectroscopy: Theory, Experiment, and Applications* (Wiley-Interscience, Hoboken, 2005).

[5] Y. Xu, *Ferroelectric Materials and Their Applications* (North-Holland, Amsterdam, 1991).

[6] A. Gronotte, *Development of New Chemical Processes to Lead-Free Piezo- and Ferroelectric Materials* (Simon Fraser University, 2006)

[7] *RT66A Standardized Ferroelectric Test System V 2.1 Operating Manual* (Radiant Technologies, Inc., 1998).

[8] C.B. Sawyer, and C.H. Tower, Phys, Rev, 35, 269 (1930).

[9] http://www.msm.cam.ac.uk/doitpoms/tlplib/ferroelectrics/measuring_pol.php

[10] http://www.sinocera.net/en/product%20pic/sensor%20d33_2.gif

Chapter 3

Lead-Free Ferroelectric Materials Derived from the $(1-x)AgNbO_3$-$xKNbO_3$ Solid Solution System

3.1 Abstract

A lead-free ferroelectric solid solution of $(1-x)AgNbO_3$-$xKNbO_3$ [$(1-x)$AN-xKN, with x = 0 - 0.12], has been prepared in the form of ceramics by solid state reaction under controlled O_2 atmosphere. It was found that with the increase of the K concentration, the Curie Temperature (T_C) decreases gradually from 342 ^oC for x = 0 to 245 ^oC for x = 0.06 and stabilizes after x > 0.06. On the other hand, the maximum dielectric permittivity (ε'_{max}) increases significantly with the increase of K concentration, i.e. ~ 7 times higher for x = 14% than for the pure AN. It was also found that P_r increases slightly when the K concentration rises from 0 to 0.07, and then increases dramatically for $x \geq 0.08$, giving rise to a maximum polarization (P_r = 8.5 μC/cm^2) at x = 0.12 at room temperature, which is ~120 times higher than that of the pure AN. The crystal chemical studies, combined with the characterization of physical properties, indicate the presence of a critical point in the vicinity of x = 8% $KNbO_3$, at which the weak ferroelectric phase

transforms into a normal ferroelectric phase in the (1-x)AN-xKN solid solution, which is induced by the substitution of K^+ for Ag^+ ion.

3.2 Introduction

Lead-based perovskites, such as $Pb(Zr,Ti)O_3$ (PZT) and $Pb(Mg_{1/3}Nb_{2/3})O_3$-$PbTiO_3$ (PMN-PT) have shown superior piezoelectric performance, and are commonly used in electromechanical transduction applications for sensor and actuators [1,2]. However, due to concerns about the toxicity of lead, there has been increasing interest in developing lead-free ferroelectric materials to reduce the environmental impact. It has been reported that the solid solution between $KNbO_3$ and $NaNbO_3$ around the morphotropic phase boundary (MPB) composition, $K_{0.5}Na_{0.5}NbO_3$ (KNN) exhibits high piezoelectric performance [3,4]. Therefore, the KNN-based compounds form a promising class of lead-free piezoelectric materials.

Much less noticed, silver niobate, $AgNbO_3$ (AN), is also an interesting lead-free ferroelectric material since it has a high Curie temperature (T_C) of about 360 ^oC [5, 6], and can be easily prepared in the form of ceramics by solid state reaction method. AN is found to have a paraelectric phase above 353 ^oC, an antiferroelectric phase between 67 and 353 ^oC, and a weak ferroelectric phase below 67 ^oC [5-9]. The weak ferroelectricity is

caused by the small ionic size of silver which gives rise to tilted octahedra on the A-site of the perovskite structure, so that A-site off-centering displacement, which would be at the origin of a long-range ferroelectric order, is suppressed [10,11]. Therefore, attempts have been made to enhance the ferroelectric performance in $AgNbO_3$ and the related systems. Recent studies have shown that elimination of the tilted octahedral can be achieved by doping with other ferroelectric material such as $LiNbO_3$ [6,12], or by applying a high electric field to reach a large polarization [13].

On the other hand, potassium niobate, $KNbO_3$ (KN), is known to be a normal ferroelectric material with a high Curie temperature T_C = 418 ^oC [14]. Single crystals of KN were reported to have good piezoelectric properties [15, 16]. However, dense ceramics of KN are difficult to prepare by conventional solid state method and sintering mainly due to the vaporization of K_2O during the sintering process. As a result, the ratio of K over Nb deviates from stochiometric, which in turn leads to impure phases and the deliquescence problem [17-19]. The solid solution of (1-*x*)AN-*x*KN with a small concentration of KN has been investigated by Kania and Lukaszewski [5, 20], however, the systematic studies of dielectric and ferroelectric properties of larger KN concentrations, as well as the possibility of phase transformation induced by the substitution of K^+ for Ag^+ ion, have been missing. In this work, the lead-free solid

solution system of (1-*x*)AN-*x*KN has been synthesized and its structure and its physical properties have been investigated in order to explore the possibility of developing a high-performance ferroelectric material on the basis of AN.

3.3 Experimental Procedure

The flow chart of the experimental procedure is shown in Figure 3.1. Ceramics of the (1-*x*)AN-*x*KN ($0 \leq x \leq 0.12$) solid solution were prepared by solid state reaction. The stoichiometric amounts of the starting chemicals, Ag_2O (99.9%), K_2CO_3 (99%), and Nb_2O_5 (99.9%) were mixed and ground thoroughly. The mixed powder was pressed into pellets and calcined at a temperature of 800 ^oC for 4 h in a controlled oxygen atmosphere. After calcination, the pellets were regrounded and repressed into pellets of 1 cm in diameter and then sintered at 1030~1100 ^oC for 2.5 h to form dense ceramics. The phase formation of the (1-*x*)AN-*x*KN solid solution was analyzed by X-ray diffraction using a Rigaku diffractometer with Cu *K*α source. The dielectric measurements were carried out by means of a computer-controlled Alpha broad-band dielectric/impedance spectrometer (Novo-control) in the frequency range of 1 kHz to 100 kHz upon cooling from 350 ^oC to -50 ^oC. The polarization-electric field (*P*-*E*) hysteresis loops were measured at room temperature using an RT66A Standard Ferroelectric Testing System (Radiant Tech.).

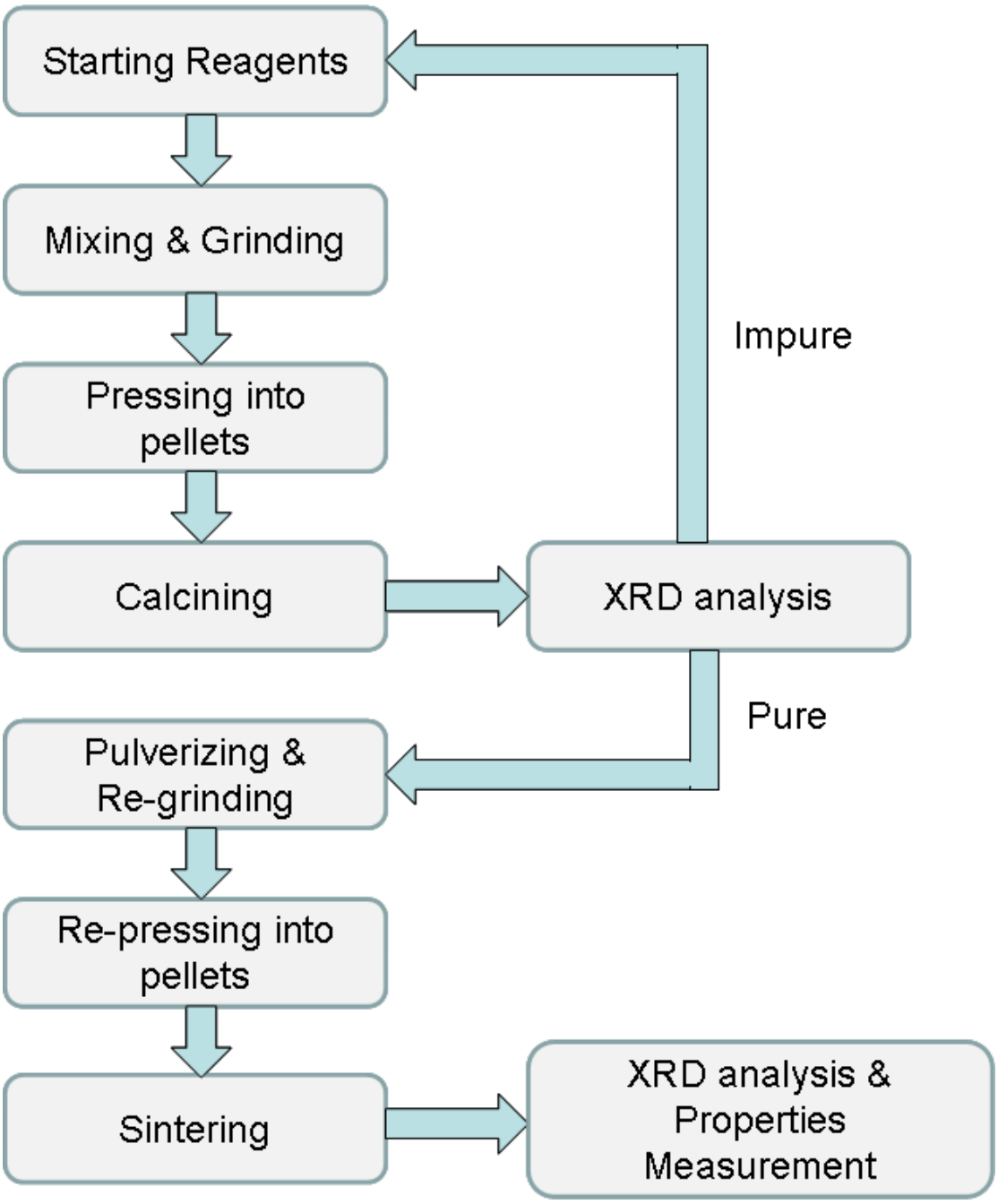

Figure 3.1: The flow chart of experimental procedure.

3.4 Results and Discussion

3.4.1 XRD Patterns and Lattice Parameters

The X-ray diffraction patterns of the sample prepared are presented in Fig. 3.2, which shows that a pervoskite phase was formed for the (1-*x*)AN-*x*KN solid solution in the concentration range of $0 \leq x \leq 0.12$. The presence of a trace amount of metallic silver phase can be found in the samples at 38^{o}. The lattice parameters of the (1-*x*)AN-*x*KN (*x*=0-0.12) ceramics were calculated based on the Pbcm space group of the $AgNbO_3$ using Peakfit software. Figure 3.3 shows the variation of orthorhombic lattice parameters (*a*, *b*, and *c*) and volume of (1-*x*)AN-*x*KN solid solution as function of KN composition *x*. It can be seen that with the increase of KN concentration, the lattice parameters *a* and *c* increase continuously, while lattice parameter *b* increases from $x = 0$ to $x = 0.08$ and then decrease at $x > 0.08$. This result suggests that a structural change in the solid solution may take place. Furthermore, since the ionic size of Ag^{+}[$r(^{VIII}Ag^{+})$=1.28 Å] is smaller than that of K^{+}[$r(^{VIII}K^{+})$=1.51 Å] [21], the increasing trend in the unit cell volume indicates that K^{+} ions have indeed entered the AN lattice to substitute Ag^{+}, thus forming a solid solution.

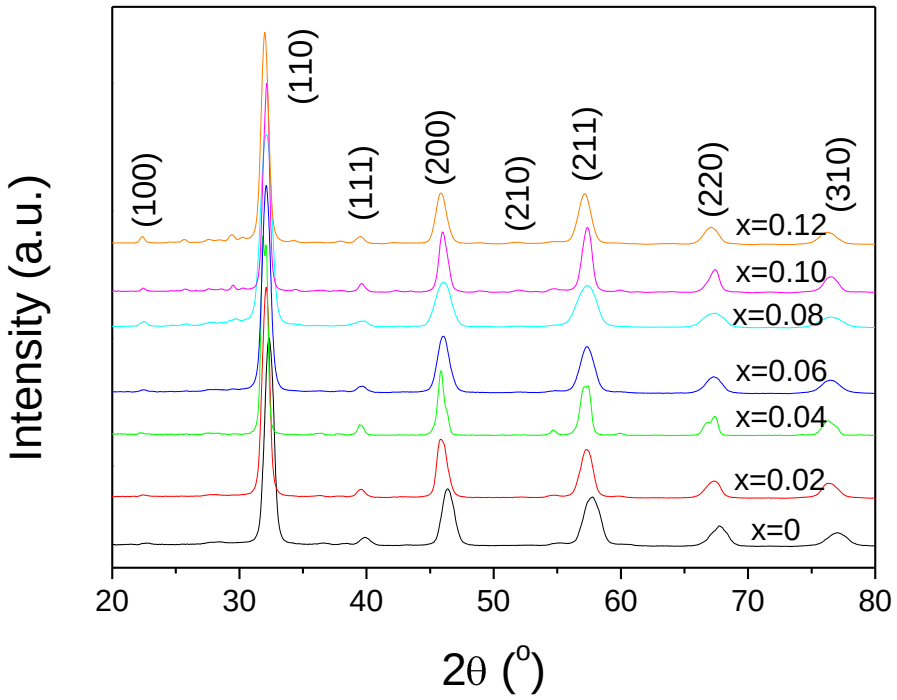

Figure 3.2: XRD patterns of the (1-*x*)AN-*x*KN ceramics (*x* = 0 - 0.12).

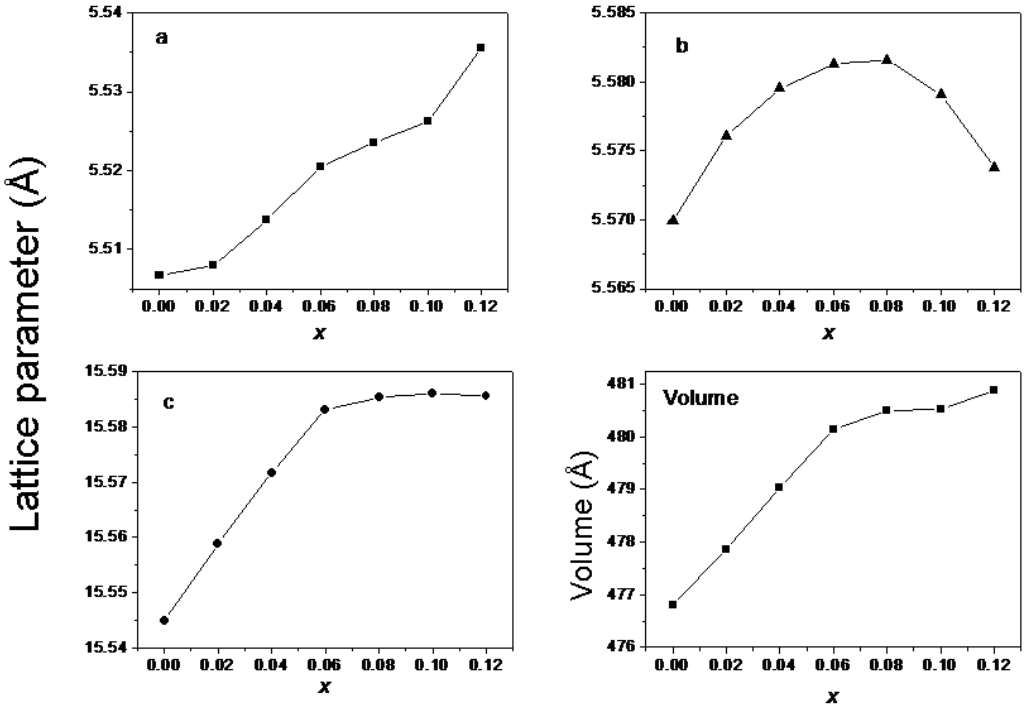

Figure 3.3: Orthorhombic lattice parameters (*a*, *b*, and *c*) and volume of the (1-*x*)AN-*x*KN (*x* = 0 – 0.12) solid solution as function of KN concentration *x*.

3.4.2 Dielectric Properties

Fig.3.4 shows the temperature dependences of the real part of dielectric permittivity (or dielectric constant, ε') and the loss tangent (tanδ) measured at the frequency *f* = 100 kHz for selected compositions. The sharp peak in the dielectric curve corresponds to the ferro-/paraelectric phase transition at T_C. It can be seen that with the increase in the potassium concentration, T_C shifts to lower temperature from 342 ^{o}C for *x* = 0 to 245 ^{o}C for *x* = 0.06, and stabilizes after $x \geq 0.06$, while the value of loss tangent increases from *x* = 0.04 to 0.06. In general, all compositions exhibit a good thermal

stability of the dielectric properties with the loss tangent smaller than 0.06 at 100 kHz over a wide temperature range between 25 and 400 ^{o}C. Interestingly, the maximum dielectric constant and room temperature dielectric constant (ε'_{max}) measured at 100 kHz are increased dramatically from AN to the 0.88AN-0.12KN ceramic (Figure 3.5), which clearly suggests that the weakly polar order in AN has been enhanced by the KN substitution, indicating that the ferroelectric phase in AN has transformed into a normal ferroelectric phase in the (1-*x*)AN-*x*KN solid solution with the substitution of KN for AN. The two other dielectric anomalies ("shoulders") correspond to the orthorhombic(M_1)-orthorhombic(M_2) (at T_1) and orthorhombic(M_2)-orthorhombic(M_3) (at T_2) phase transitions in AN. It is interesting to note that these two phase transitions merge into one peak, as a result of the increased potassium concentration in the solid solution. According to the geometric study of perovskite compounds by Galasso [22], silver niobate has an average size of unit cell in between the displacive-type ferroelectric potassium niobate and octahedral tilting-type anitferroelectric sodium niobate. A competition between parallel and anitparallel Nb^{5+} ions may give rise to the diffused weak-ferroelectric M_1-M_2 and anitferroelectric M_2- M_3 phase transitions [23]. Hence, with the potassium ion substituting for Ag^{+}, one can expect that the octahedral tilting of AN is gradually shifted towards a displacive-type ferroelectric.

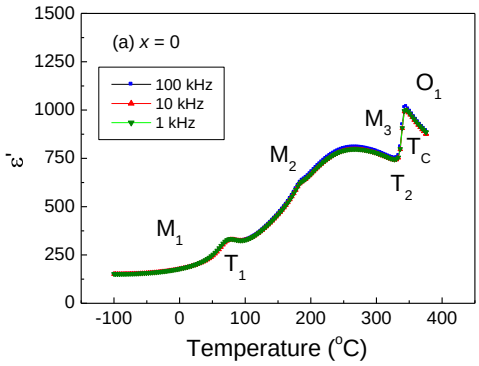
(a) x = 0
100 kHz
10 kHz
1 kHz
M1
T1
M2
M3
O1
TC
T2
ε'
Temperature (°C)

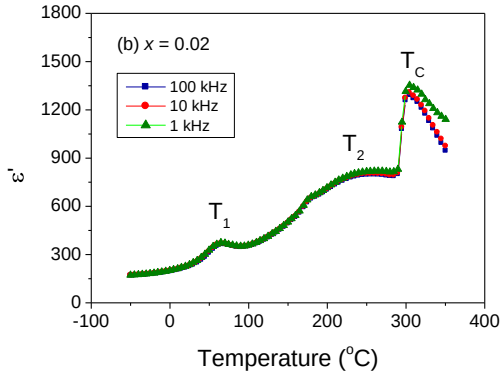
(b) x = 0.02
100 kHz
10 kHz
1 kHz
T1
T2
TC
ε'
Temperature (°C)

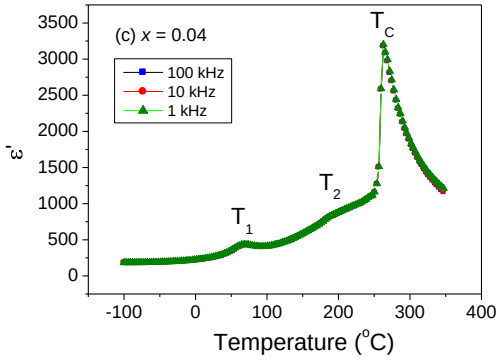
(c) x = 0.04
100 kHz
10 kHz
1 kHz
T1
T2
TC
ε'
Temperature (°C)

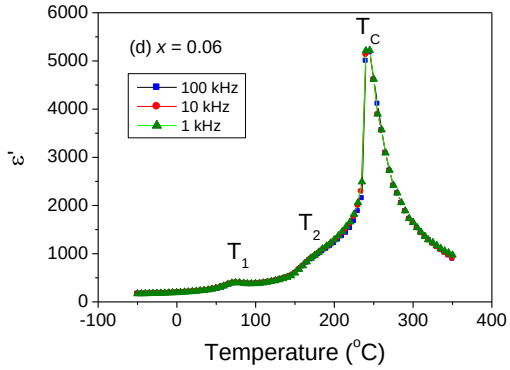
(d) x = 0.06
100 kHz
10 kHz
1 kHz
T1
T2
TC
ε'
Temperature (°C)

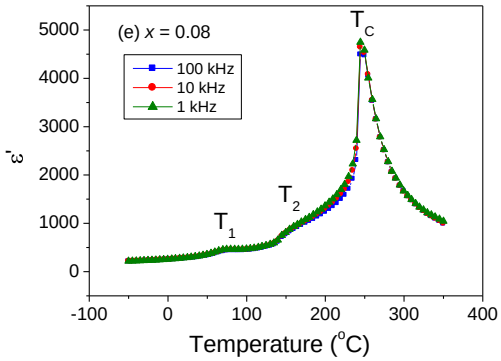
(e) x = 0.08
100 kHz
10 kHz
1 kHz
T1
T2
TC
ε'
Temperature (°C)

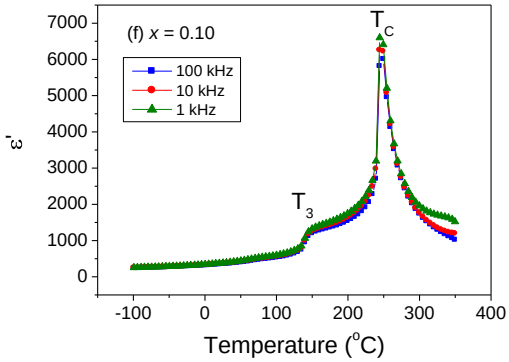
(f) x = 0.10
100 kHz
10 kHz
1 kHz
T3
TC
ε'
Temperature (°C)

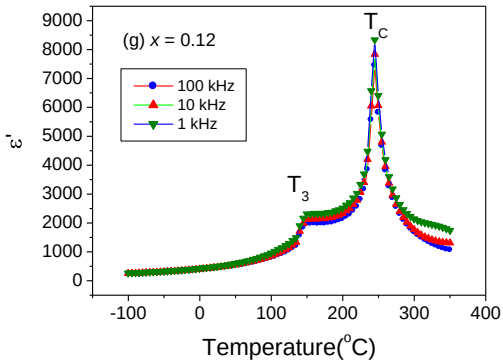
(g) x = 0.12
100 kHz
10 kHz
1 kHz
T3
TC
ε'
Temperature(°C)

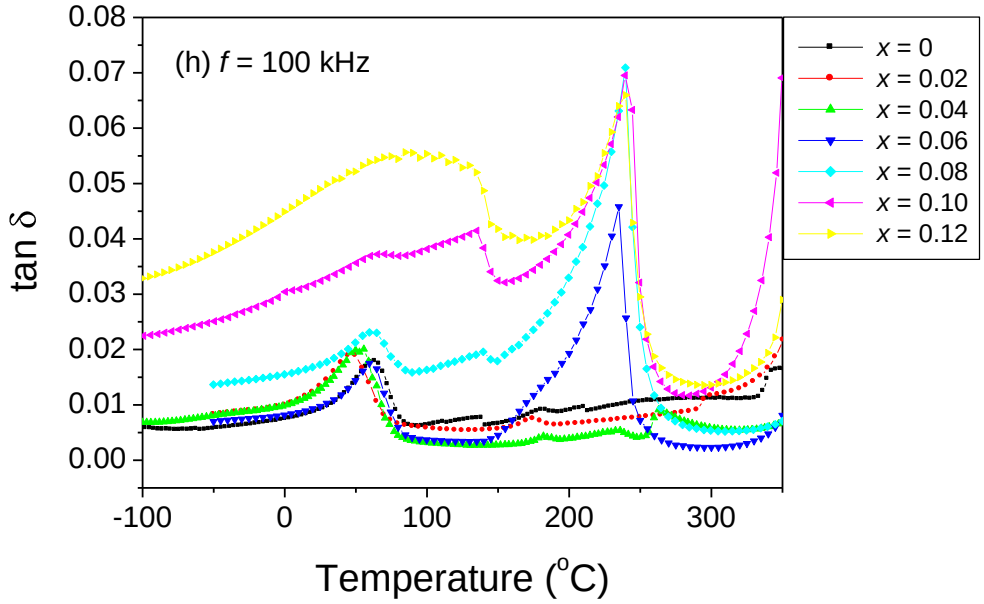

Figure 3.4: Temperature dependences of the dielectric constant (a-g) and the loss tangent (h) of the (1-*x*)AN-*x*KN ceramics (*x* = 0 - 0.12). T_C, T_1, T_2, and T_3 indicate the Curie temperature, the phase transition temperature between orthorhombic M_1 and M_2 phases, the phase transition temperature between orthorhombic M_2 and M_3 phases, and the new ferroelectric phase transition temperature, respectively.

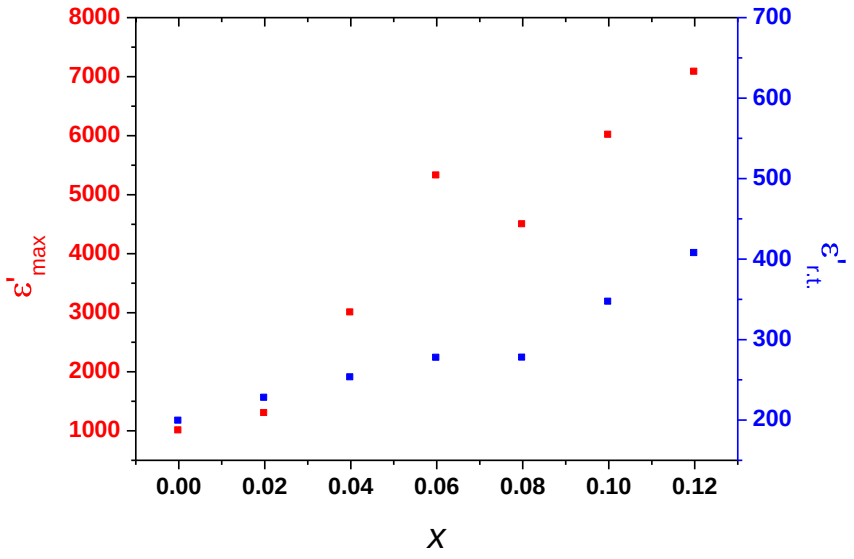

Figure 3.5: Room temperature dielectric constant ($\varepsilon'_{r.t}$) and maximum dielectric constant (ε'_{max}) of the (1-*x*)AN-*x*KN (*x* = 0 - 0.12) ceramics measured at *f* = 100 kHz.

3.4.3 Ferroelectric Properties

The polarization-electric field (P-E) hysteresis loops displayed on the (1-*x*)AN-*x*KN ceramics of various compositions at room temperature at the frequency of 20 Hz are shown in Fig 3.6. As expected, very weak ferroelectricity with a very small spontaneous polarization is displayed in pure $AgNbO_3$. When the potassium amount is under $x = 0.08$, the P-E loops still remain slim with small remnant polarization (P_r). With further increase of KN to $x \geq 0.08$, the P-E loops become more hysteretic and P_r undergoes a sharp increase, reaching a value of $P_r = 8.05$ μC/cm^2 for u $x = 0.12$ under an applied electric field of ±30 kV/cm (Fig 3.7). This indicates that a new macroscopic ferroelectric state has been induced by the substitution of KN for AN. For the samples with $x > 0.12$, the impurity phases cause the AN-KN ceramics to become conductive, giving rise to degraded *P-E* loops (not shown). Referring to the first principle study based on 5-atoms and 40-atoms unit cell calculations of $AgNbO_3$ by Gringberg and Rappe [24], large octahedral rotations create short covalent Ag-O bonds with small Ag off-center displacements (0.1 Å) in the 40-atoms unit cell. Consequently, the polarization of $AgNbO_3$ is inhibited and weak ferroelectricity is present at room temperature. In contrast, the octahedral rotations are hindered in the 5-atoms unit cell, the short covalent Ag-O bond is achieved mainly through off-center displacement of Ag (0.5 Å).

Substitution of a lager A-site cation into $AgNbO_3$ favours the elimination of octahedral tilting. This is believed to be the reason for the development of the macroscopic ferroelectric phase in the (1-*x*)AN-*x*KN by the substitution of the larger K^+ for the smaller Ag^+ ion, giving rise to the appearance of large polarization observed in *P*-*E* loops.

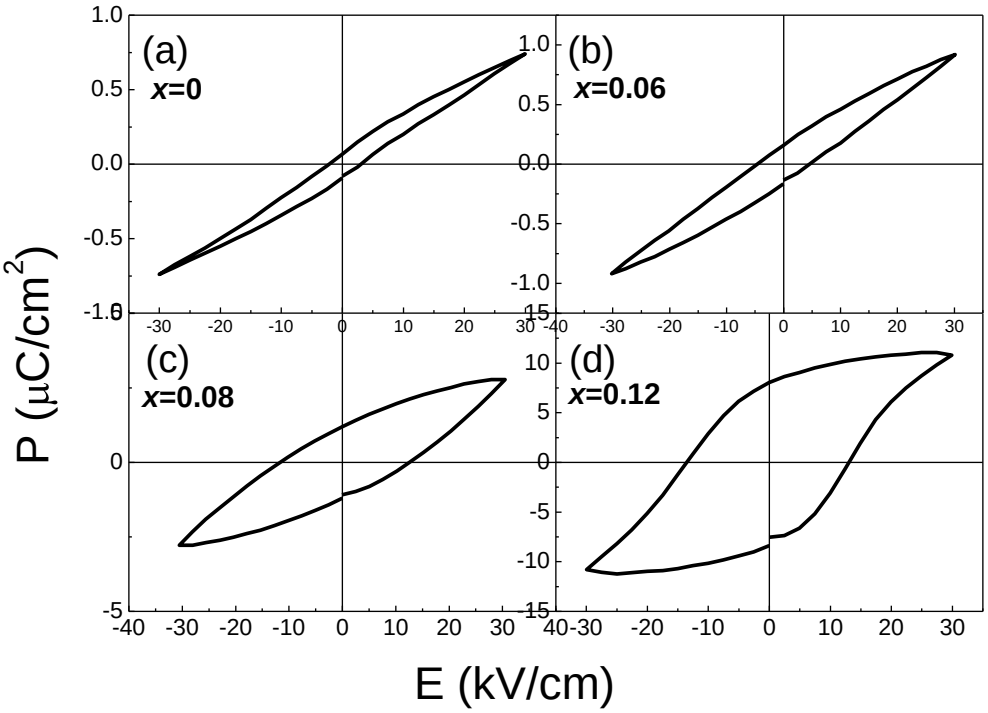

Figure 3.6: Polarization-electric field (*P*-*E*) hysteresis loops displayed on the (1-*x*)AN-*x*KN (*x* = 0, 0.06, 0.08, 0.12) ceramics at room temperature at *f* = 20 Hz and under an electric field of ±30 kV/cm.

.

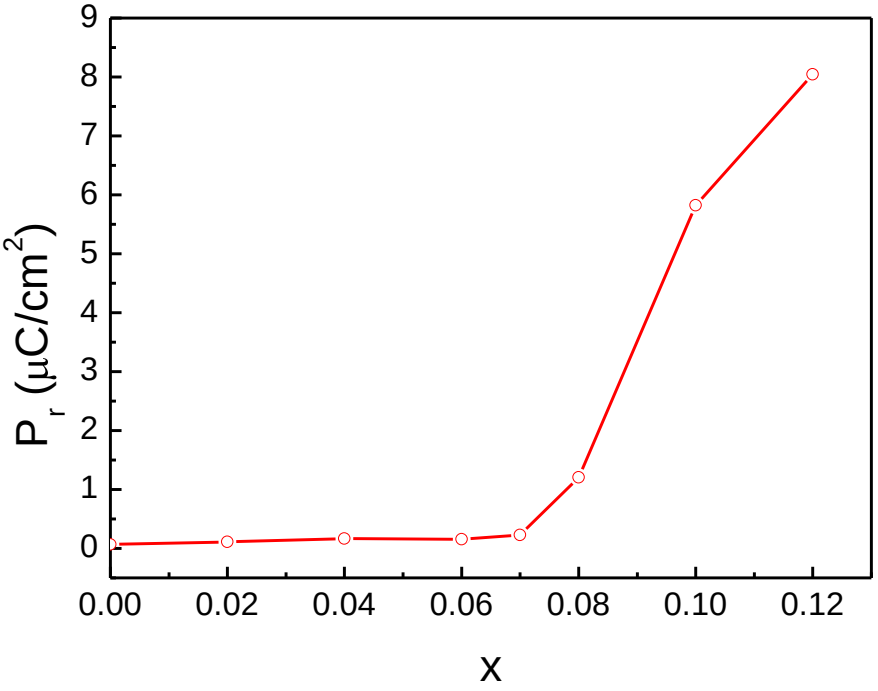

Figure 3.7: Remnant polarization (P_r) as a function of the potassium concentration measured on the (1-*x*)$AgNbO_3$-*x*$KNbO_3$ (x=0 - 0.12) ceramics from the hysteresis loop in Figure 3.6.

3.5 Conclusions

The ceramics of the lead-free (1-*x*)AN-*x*KN ($0 \leq x \leq 0.12$) solid solution have been synthesized by solid state reaction in controlled oxygen atmosphere. The substitution of K^+ for Ag^+ is found to cause T_C to decrease gradually from 342 ^oC in $x = 0$ to 245 ^oC in $x = 0.06$. The dielectric studies show a significant increase in ε'_{max} with the increase of K^+ concentration, i.e. ~ 7 times higher for $x = 0.12$ than for the pure AN. Moreover, it is found that the remnant polarization increases slightly when K^+

concentration rises from 0 to 0.07, and more dramatically for $x \geq 0.08$, giving rise to a significant remnant polarization value of P_r = 8.06 μC/cm^2 at x = 0.12 at room temperature, which is ~120 times higher than that of the pure AN. It is found that weak ferroelectricity in $AgNbO_3$ is transformed into a normal ferroelectric phase in the (1-x)AN-xKN solid solution in the vicinity of x= 8%. Such a ferroelectric state induced by the K^+ substitution can be attributed to the suppression of oxygen octahedral tilting in $AgNbO_3$. Therefore, the dielectric and ferroelectric properties are greatly improved in the K-modified $AgNbO_3$ ceramics, making them promising lead-free ferroelectric material for potential applications.

References

[1] G. H. Haertling, J. Am. Ceram. Soc. **82,** 797 (1999).

[2] L. E. Cross, Ferroelectrics **76,** 241 (1987).

[3] G. H. Haertling, J. Am. Ceram. Soc. **50,** 329 (1967).

[4] R. E. Jaeger and L. Egerton, J. Am. Ceram. Soc. **45,** 209 (1962).

[5] A. Kania, J. Phys. D. **34,** 1447 (2001).

[6] A. Kania and S. Miga, Mater. Sci. Eng. B-Solid State Mater. Adv. Technol. **86,** 128 (2001).

[7] K. H. Ryu, J. A. Cho, T. l. Song, M. H. Kim, S. S. Kim, H. S. Lee, S. J. Jeong, J. S. Song, and K. S. Choi, Ferroelectrics **338**, 57 (2006).

[8] A. Kania, Ferroelectrics **205**, 19 (1998).

[9] A. Ratuszna, J. Pawluk, and A. Kania, Phase Transitions **76**, 611 (2003).

[10] M. Pawelczyk, Phase Transitions **8,** 273 (1987).

[11] M. Verwerft, D. Vandyck, V. A. M. Brabers, J. Vanlanduyt, and S. Amelinckx, Phys. Status Solidi A-Appl. Res. **112,** 451 (1989).

[12] Y. Sakabe, T. Takeda, Y. Ogiso, and N. Wada, Jpn. J. Appl. Phys. Part 1 **40,** 5675 (2001).

[13] D. S. Fu, M. Endo, H. Taniguchi, T. Taniyama, and M. Itoh, Appl. Phys. Lett. **90,**

3 (2007).

[14] H. Birol, D. Damjanovic, and N. Setter, J. Am. Ceram. Soc. **88,** 1754 (2005).

[15] K. Nakamura, T. Tokiwa, and Y. Kawamura, J. Appl. Phys. **91,** 9272 (2002).

[16] S. Wada, A. Seike and T. Tsurumi: Jpn. J. Appl. Phys. **40**, 5690 (2001).

[17] T. Wada, A. Suzuki, and *T*. Satio, Jpn. J. Appl. Phys. **45**, 7431 (2006).

[18] S. Tashiro, H. Nagamatsu and K. Nagata, Jpn. J. Appl. Phys. **41,** 7113 (2002).

[19] A. Reisman, F. Holtzberg, S. Triebwasser, and M. Berkenblit, J. Am. Ceram. Soc. **78,** 719 (1956)

[20] M. Lukaszewski, Ferro. Lett. **44**, 319 (1983).

[21] R. D. Shannon, Acta Crystallogr. Sect. A **32,** 751 (1976).

[22] F. S. Galasso, *Structure, Properties and Preparation of Perovskite Type Compounds* (Oxford Eng.: Pergamon, 1969).

[23] A. Kania and J. Kwapulinski, J. Phys.-Condes. Matter **11,** 8933 (1999).

[24] I. Grinberg and A. M. Rappe, App. Phys. Lett. **85,** 1760 (2004).

Chapter 4

Lead-Free Ferroelectric Materials Derived from the $(1-x)AgNbO_3$- $xK_{0.5}Na_{0.5}NbO_3$ Solid Solution System

4.1 Abstract

A new lead-free solid solution of $(1-x)AgNbO_3$-$xK_{0.5}Na_{0.5}NbO_3$ [$(1-x)$AN-xKNN] with x = 0 - 0.40, has been prepared in the form of ceramics. The substitution of $(K_{0.5}Na_{0.5})^+$ for Ag^+ greatly enhances both dielectric and ferroelectric properties of $AgNbO_3$. With increasing KNN content, the maximum dielectric constant increases significantly, i.e. to a value that is ~ 8.5 times higher for x = 0.12 than for the pure AN, and the Curie temperature decreases from 345 ^oC for x = 0 to 250 ^oC for x = 0.10 and then increases again from 250 to 280 ^oC for x = 0.12 - 0.40. It is also found that the remnant polarization (P_r) increases dramatically, giving rise to a maximum polarization (P_r = 6.5 $\mu C/cm^2$) at x = 0.30. Such an enhanced ferroelectricity is attributed to the establishment of a long-range macroscopically polar state induced by the substitution of KNN for AN. The symmetry of induced ferroelectric phase in the solid solution is refined to be of the polar space group $Pbc2_1$.

4.2 Introduction

Silver niobate, $AgNbO_3$ (AN), is one of environmentally friendly lead-free materials that has attracted renewed interest due to its high ferroelectric Curie temperature (T_C) of about 353 ^oC [1, 2]. AN exhibit a paraelectric phase above 353 ^oC, an antiferroelectric phase between 67 and 353 ^oC, and a weak ferroelectric phase below 67 ^oC [1-6]. The low-temperature weak ferroelectric and antiferroelectric phases are related to the parallel and antiparallel displacements of the Nb^{5+} ions, repeatively, within the tilted oxygen octahedral sites. The phase transitions in AN are difficult to detect by x-ray diffraction [1, 2, 7], probably because of the relatively weak structural distortion associated, which in turn results in weak ferroelectricity. Several approaches were proposed to suppress the oxygen octahedral tilting with a view to restoring the potentially strong ferroelectricity in $AgNbO_3$ [8-11]. Recent studies have shown that the octahedral tilting can be eliminated by doping with other ferroelectric materials such as $LiNbO_3$ [8, 12], or by applying a high electric field to induce a large polarization [11].

Compounds of the alkali niobate family, such as $LiNbO_3$ (LN), $NaNbO_3$ (NN) and $KNbO_3$ (KN), provide possible candidates to form solid solutions with AN. Kania reported the dielectric and ferroelectric properties of the alkali niobate solid solutions

with AN [1]. On the other hand, potassium sodium niobate, $K_{0.5}Na_{0.5}NbO_3$ (KNN), a solid solution of the two alkali niobate compounds, is known to be a promising lead-free piezo- and ferroelectric material, because it exhibits excellent piezoelectric properties (with piezoelectric coefficient d_{33} = 160 pC/N and the planar electromechanical coupling factor k_p = 47%) in the form of hot-pressed ceramics [13, 14]. However, the synthesis of highly dense KNN ceramics by conventional sintering methods encounter the deliquescence problem, and as a result, poorly densified ceramics with impurity phases are often obtained [13 -15]. Recent work in our group has shown that the substitution of Ag^+ ions for the complex $(Na_{0.5}K_{0.5})^+$ ions can improve the relative density of KNN ceramics, with the relative density reaching 94% by a conventional solid state reaction under ambient pressure, and moreover, the piezoelectric properties are also enhanced significantly (with d_{33} = 186 pC/N for the 0.82KNN-0.18AN ceramics) [16]. However, little has been known about the solid solution on the AN-rich side.

The objective of this work was to synthesize the solid solution of (1-*x*)AN-*x*KNN on the AN-rich side and to investigate the structural and dielectric, ferroelectric, and piezoelectric properties of this lead-free material, in particular the structural transformation resulting from the chemical substitution of KNN for AN.

4.3 Experimental Procedure

Ceramics of the (1-*x*)AN-*x*KNN ($0 \leq x \leq 0.50$) solid solution were prepared by solid state reaction. The stoichiometric amounts of the starting materials, Ag_2O (99.9%), K_2CO_3 (99%), $Na_2CO_3 \cdot H_2O$ (99.5%), and Nb_2O_5 (99.9%), were mixed and ground thoroughly. The mixed powder was pressed into pellets and calcined at a temperature of 850 ^oC for 4 hrs in an oxygen atmosphere. After calcination, the pellets were reground and repressed into pellets of 1 cm in diameter and then sintered at 1050~1100 ^oC for 4 hrs to form dense ceramics. A Rigaku diffractometer with Cu *K*α source was used to check the formation of the (1-*x*)AN-*x*KNN solid solution phase. Gold layers were deposited by sputtering on the polished circular surfaces of the ceramics as electrodes for electric characterization. Dielectric measurements were carried out by means of a Solartron 1260 Impedance Analyzer combined with a 1296 Dielectric Interface in the frequency range of 100 Hz to 100 kHz upon cooling from 550 ^oC to 25 ^oC. The polarization-electric field (*P*-*E*) hysteresis loops were measured at room temperature by an RT66A Standard Ferroelectric Testing System (Radiant Tech.).

4.4 Results and Discussion

4.4.1 Structure and Phase Analysis

Fig.4.1 shows the X-ray diffraction patterns of the (1-*x*)AN-*x*KNN ceramics, with compositions of $x = 0 – 0.4$. A pure perovskite phase of orthorhombic symmetry is found in the ceramics with lower contents of KNN ($x < 0.30$). With $x \geq 0.30$, a small amount of metallic silver phase and other secondary phases, such as $Ag_2Nb_4O_{11}$, was found to be present, indicating that the solubility limit of the (1-*x*)AN-*x*KNN solid solution lies around $x = 0.30$.

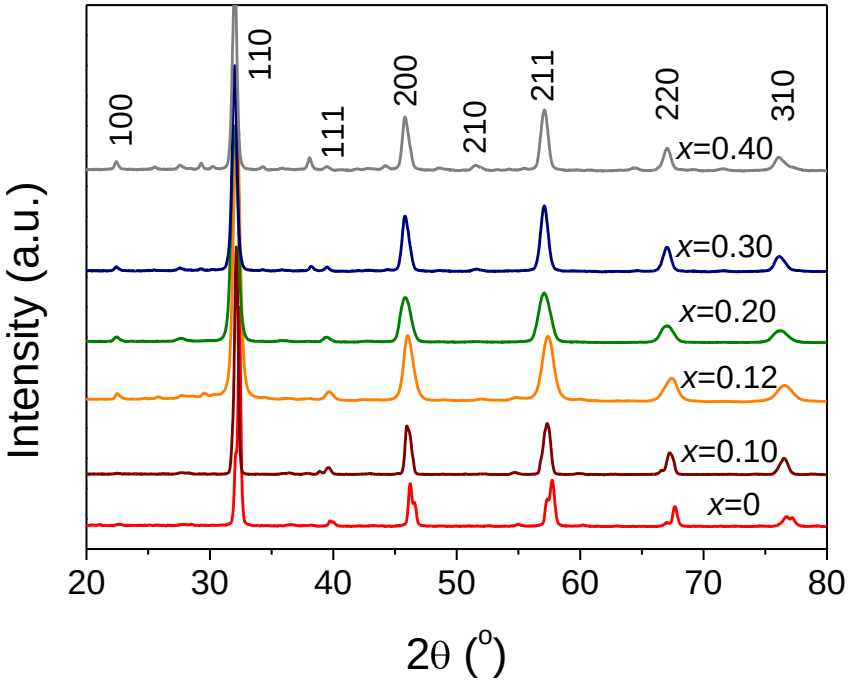

Figure 4.1: X-ray diffraction patterns of the (1-*x*)AN-*x*KNN ($x = 0 – 0.40$) ceramics.

Figure 4.2 shows the variation of the orthorhombic lattice parameters (*a*, *b*, and *c*) and volume of the (1-*x*)AN-*x*KNN solid solution as a function of the KNN concentration

x. The lattice parameters were calculated based on the Pbcm space group of the $AgNbO_3$ structure using Peakfit software. It can be seen that with the increase of KNN content, the lattice parameters *a* and c increase continuously from *x*=0 to *x*=0.20 and then stabilize at *x* > 0.20. This result indicates that the larger A-site ion, $(K/Na)^+$ with the ionic size [$r(^{VIII}K^+)$=1.51 Å, $r(^{VIII}Na^+)$=1.18 Å] has indeed replaced Ag^+ [$r(^{VIII}Ag^+)$=1.28 Å] [17] in $Ag_{1-x}(Na_{0.5}K_{0.5})_xNbO_3$, confirming the formation of the solid solution. On the other hand, the lattice parameter *b* decreases first and increases again noticeably at *x* = 0.12. This V-shaped trend suggests a possible sudden structural change in the solid solution with increasing KNN substitution. The origin of such a structural phase transition will be discussed later in Sec 4.4.5, which involves the elimination of oxygen octahedral tilting.

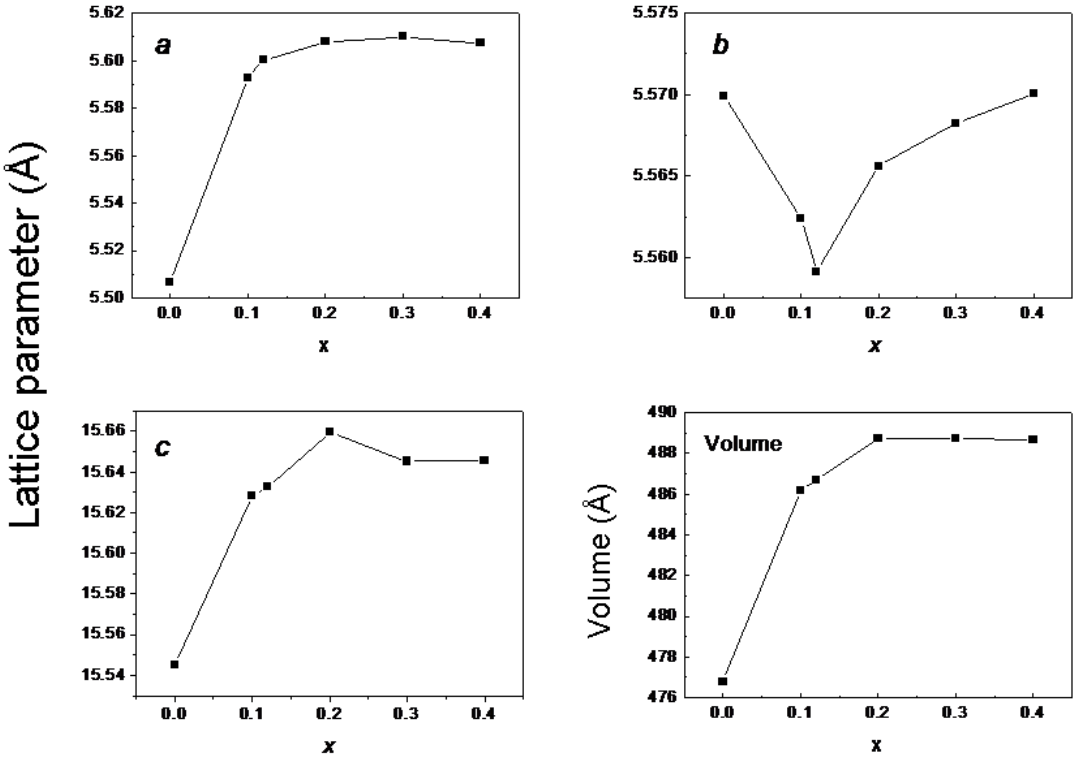

Figure 4.2: Orthorhombic lattice parameters (*a*, *b*, and *c*) and volume of the (1-*x*)AN-*x*KNN (*x* = 0 – 0.40) solid solution as function of KNN concentration *x*.

4.4.2 Dielectric Properties

The variations of the real part of the dielectric permittivity (or dielectric constant, ε'), and loss tangent (tan δ) of the (1-*x*)AN-*x*KNN ceramics as a function of temperature measured at the frequencies of 1, 10, and 100 kHz are presented in Fig. 4.3. The maximum permittivity indicates the ferro-paraelectric phase at the Curie temperature T_C. As can be seen in Figure 4.3 and 4.4, T_C shifts to a lower temperature as the amount

of KNN substitution increases, i.e., from 345 ^{o}C at x = 0 to 250 ^{o}C at x = 0.10. Interestingly, with a further increase of KNN, T_C increases again from 250 ^{o}C to 280 ^{o}C at x = 0.40. This result suggests a phase transition occurred in x = 0.12. In contrast to the decrease of T_C with KNN substitution, the maximum dielectric permittivity (ε'_{max} measured at 100 KHz) is increased dramatically from 998 for pure AN up to 8143 for the 0.80AN-0.20KNN ceramic. In addition, the dielectric permittivity at room temperature also increases with increasing KNN amount and reaches a maximum at x = 0.20 and saturates beyond this concentration (see Figure 4.5). The increases of maximum permittivity and room temperature permittivity in AN-KNN can be attributed to the incorporation of KNN which favours normal ferroelectric behavior in the solid solution. Moreover, it should be noted that the two dielectric peaks originally corresponding to the orthorhombic(M_1)-orthorhombic(M_2) (at T_1) and orthorhombic(M_2)-orthorhombic(M_3) (at T_2) phase transitions at 78 and 264 ^{o}C, respectively, in AN, merge into one peak (T_3)when $x \geq 0.12$. All compositions exhibit a good thermal stability of the dielectric properties with the loss tangent smaller than 0.06 at 100 kHz over a wide temperature range between 25 and 400 ^{o}C.

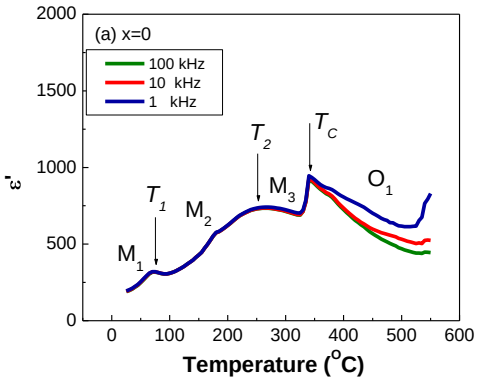
(a) x=0
100 kHz
10 kHz
1 kHz
ε'
Temperature (°C)
M1
T1
M2
T2
M3
TC
O1

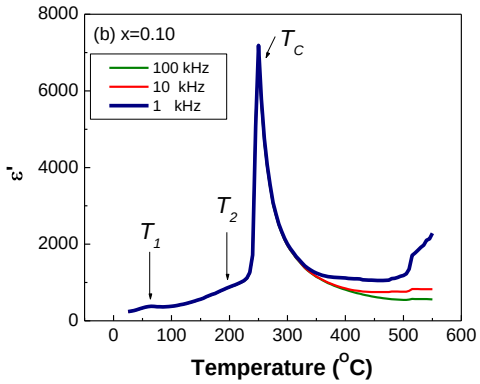
(b) x=0.10
100 kHz
10 kHz
1 kHz
ε'
Temperature (°C)
T1
T2
TC

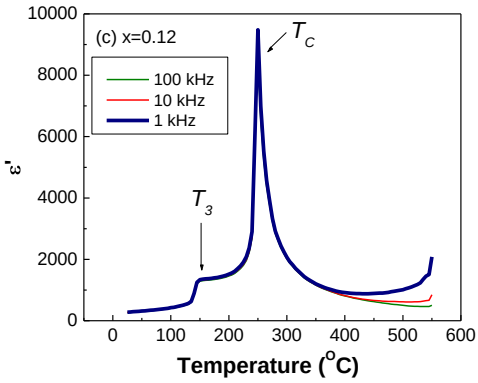
(c) x=0.12
100 kHz
10 kHz
1 kHz
ε'
Temperature (°C)
T3
TC

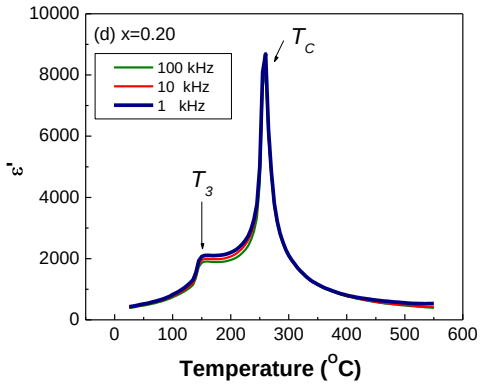
(d) x=0.20
100 kHz
10 kHz
1 kHz
ε'
Temperature (°C)
T3
TC

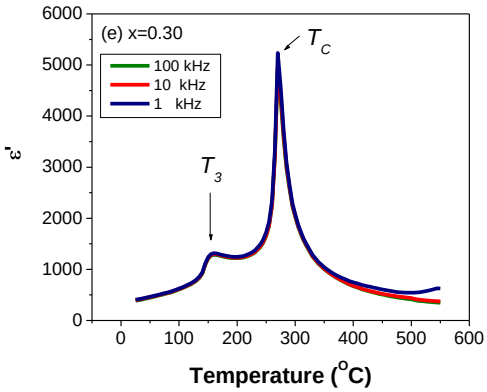
(e) x=0.30
100 kHz
10 kHz
1 kHz
ε'
Temperature (°C)
T3
TC

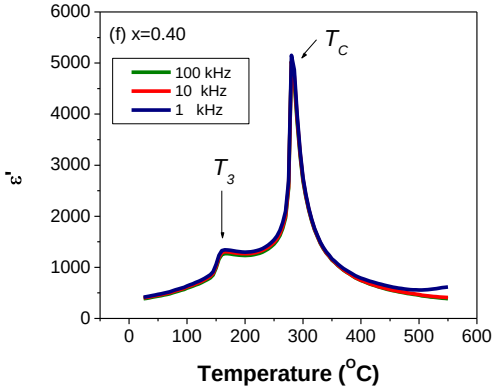
(f) x=0.40
100 kHz
10 kHz
1 kHz
ε'
Temperature (°C)
T3
TC

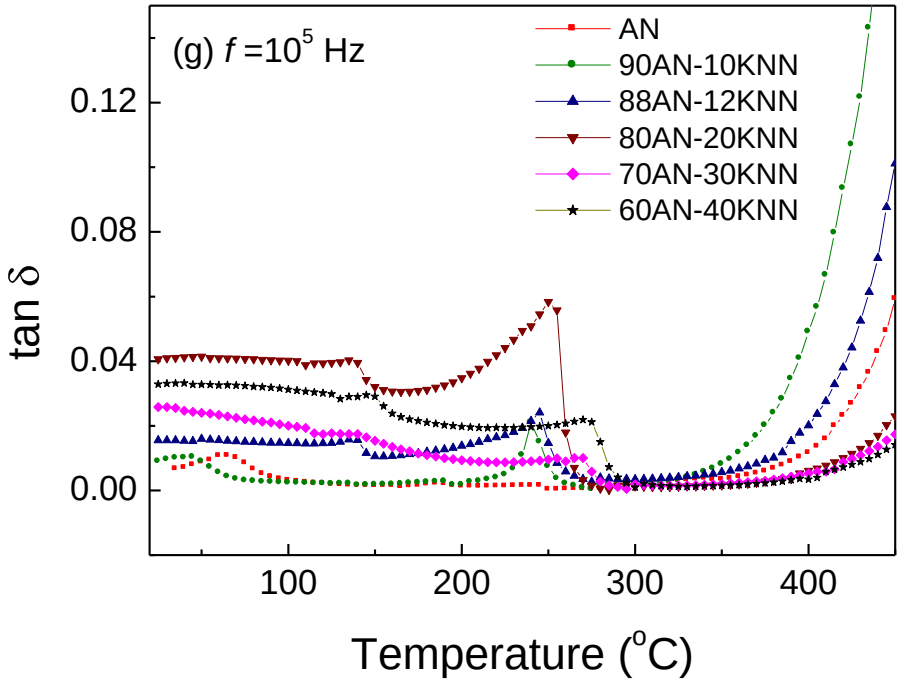

Figure. 4.3: Temperature dependences of the real parts of dielectric permittivity (ε') (a-f), and the loss tangent (tan δ) (g) of the (1-*x*)AN-*x*$K_{0.5}$NN (*x* = 0 – 0.40) ceramics measured at 10^5 Hz. T_C, T_1, T_2, and T_3 indicate the Curie temperature, the phase transition temperature between orthorhombic M_1 and M_2 phases, the phase transition temperature between orthorhombic M_2 and M_3 phases, and the new ferroelectric phase transition temperature, respectively.

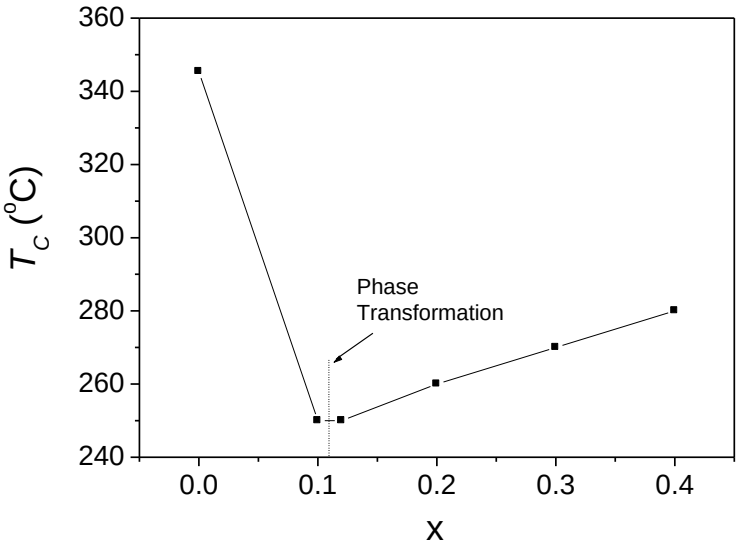

Figure 4.4: Variation of Curie temperature (T_C) of (1-*x*)AN-*x*KNN (*x* = 0 – 0.40).

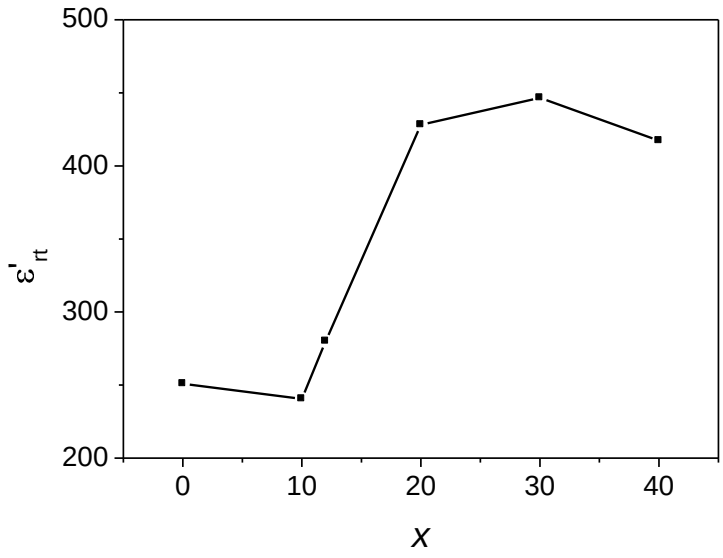

Figure 4.5: Room-temperature dielectric permittivity of (1-*x*)AN-*x*KNN (*x* = 0 – 0.40) ceramics measured at 10^5 Hz.

4.4.3 Ferroelectric Properties

The polarization versus electric field (*P*-*E*) hysteresis loops for the (1-*x*)AN-*x*KNN ceramics of various compositions measured at room temperature at the frequency of 10 Hz are shown in Fig. 4.6. The pure AN and 0.90AN-0.10KNN samples exhibit slim hysteresis loops and their remanent polarization (P_r) values are very small (< 0.20 μC/cm^2), suggesting a weak ferroelectric behavior. With the further increase of KNN content to $x \geq 0.12$, the *P*-*E* loops open up and become more hysteretic. Moreover, P_r increases dramatically to a value of P_r = 6.5 μC/cm^2 under an applied electric field of ± 20 kV/cm (Figs. 4.6 and 4.7). These results suggest that the substitution of KNN has induced a new macroscopic ferroelectric state from the weak ferroelectric state in pure AN. Since the average ionic size of K^+ and Na^+ [$r(^{VIII}K^+)$ = 1.51 Å, $r(^{VIII}Na^+)$ = 1.18 Å] is larger than that of Ag^+ [$r(^{VIII}Ag^+)$ = 1.28 Å] [17], the substitution of the larger $(K/Na)^+$ ion for Ag^+ on the A-site of the perovskite structure is expected to unlock the tilting of oxygen octahedrons, leading to the off-centered displacement of Ag^+ and Nb^{5+} ions and thereby an enhanced ferroelectricity. In addition, the normal untilted oxygen octahedral structure also favours the parallel Nb^{5+} displacement, which is a predominant mechanism for the displacive-type ferroelectricity [18, 19].

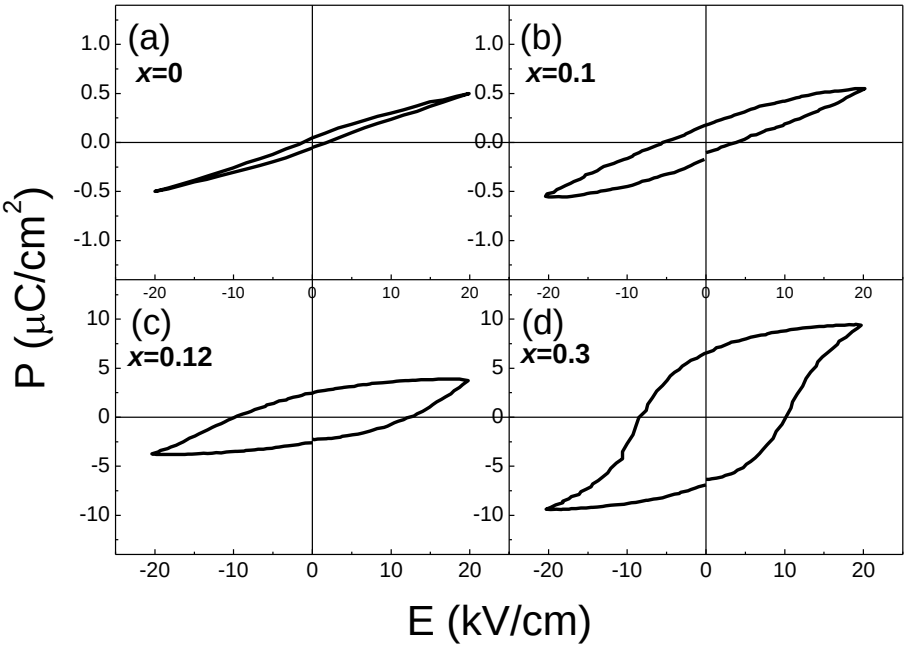

Figure 4.6: Room-temperature polarization-electric field *(P-E)* hysteresis loops displayed on the (1-*x*)AN-*x*KNN ceramics of (a) *x* = 0, (b) *x* = 0.10, (c) *x* = 0.12, and (d) *x* = 0.30, at *f* = 10 Hz.

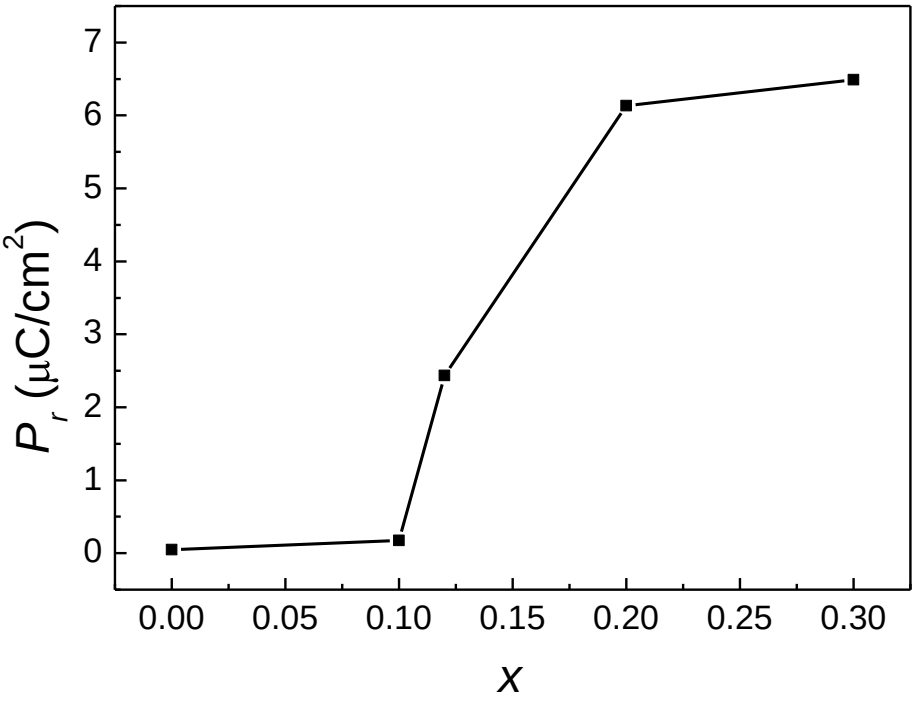

Figure 4.7: Room-temperature remnant polarization (P_r) as a function of the KNN concentration for the (1-*x*)AN-*x*KNN (*x* = 0 - 0.30) ceramic, deduced from the hysteresis loop in Fig 4.6 (*f* = 10 Hz, E = ±20 kV/cm).

4.4.4 Piezoelectric Properties

The piezoelectric coefficient d_{33} was measured in the ceramics poled at room temperature. Figure 4.8 gives the variation of the d_{33} values as a function of composition *x*. It can be seen that pure AN and 0.90AN-0.10KNN samples exhibit very weak piezoelectricity, consistent with their weak ferroelectricity. However, with further increase of KNN substitution amount, the d_{33} value undergoes a jump and reaches to 60

pC/N for 0.80AN-0.20KNN ceramic, indicating significant piezoelectric effect. Such an abrupt increase in d_{33} suggests that a long-range polar state has been induced in the (1-*x*)AN-*x*KNN solid solution by the substitution of KNN for AN. The decrease of d_{33} in 0.70AN-0.30KNN and 0.60AN-0.40KNN samples may be due to the poorer ceramic quality associated with the impure phases compared to 0.80AN-0.20KNN ceramic.

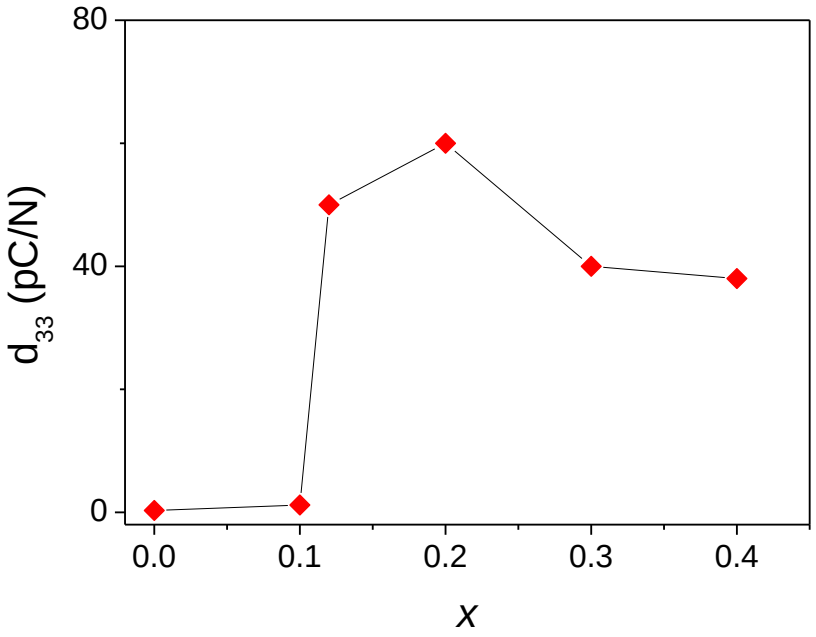

Figure 4.8: Variation of the piezoelectric coefficient (d_{33}) of the (1-*x*)AN-*x*KNN (*x* = 0 - 0.40) ceramics as a function of the composition *x*.

4.4.5 Structural Analysis of the Ferroelectric Phase

The powder diffraction pattern obtained from the XRD measurement is used to perform the structural analysis of (1-*x*)AN-*x*KNN solid solution in order to identify the

symmetry and depict the crystal lattice of the induced ferroelectric phase, and to provide a better understanding of the molecular origin of the induced ferroelectric phase transition and the relationship between the structure and ferro- and piezoelectric properties. The structural determination of the 0.80AN-0.20KNN composition was carried out by using the Rietveld refinement method with Powdercell software. The structure model built in this refinement is based on the data obtained from the crystal structure of $Li_{0.02}Na_{0.98}NbO_3$ [20]. Table 4.1 summarizes the atomic positions in the refined structure. The result of the refinement indicates that at room temperature the 0.80AN-0.20KNN solid solution adopts an orthorhombic $Pbc2_1$ symmetry with the polar space group. Reasonable R-factor values, R_P = 13.23%, R_{WP} = 25.74%, and R_{exp} = 1.5% are obtained. The R_P index indicates the agreement between the structure model adopted and the real structure. R_{WP} index indicates the weighted profile factor. R_{exp} index indicates the expected profile residual. The schematic view of the orthorhombic structure of 0.80AN-0.20KNN composition is shown in Figure 4.9, where the octahedral sites are highlighted.

The symmetry of the polar phase ($Pbc2_1$) in the (1-*x*)AN-*x*KNN (*x* > 0.10) solid solution is different from the non-polar orthorhombic symmetry Pbcm of $AgNbO_3$, which confirms that incorporation of KNN into the lattice of AN indeed changes the crystal structure, from a centro-symmetric and non-polar group to a non-centrosymmetric and

polar group. This chemically induced phase transition is accompanied by a transformation of properties from weak ferroelectricity in $AgNbO_3$ to normal ferroelectricity in the AN-KNN solid solution, as the polar group $Pbc2_1$ allows a spontaneous polarization and thus ferroelectricity. From a structural point of view, AN exhibits a tilting of the oxygen octahedrons because of the small size of Ag^+ ions. Associated with this structure, the displacement of Nb^{5+} ion is limited, as shown in Figure 4.10. Consequently, AN adopts the Pbcm symmetry with the centrosymmtric point group. The substitution of KNN for AN eliminates oxygen octahedral tilting because of the fact that the complex $(K/Na)^+$ ions are larger than Ag^+, making the perovskite structure more stable. The elimination of oxygen octahedral tilting in 0.80AN-0.20KNN allows more room for the Ag^+ and Nb^{5+} displacement, which unlocks the ferroelectricity in the solid solution. These structural features of the non-centrosymmetric and polar group $Pbc2_1$ explain the structural origin of the induced ferroelectricity in the AN-KNN solid solution.

Table 4.1: Atomic positions of 0.80AN-0.20KNN solid solution refined in the perovskite structure of the orthorhombic symmetry ($Pbc2_1$).

Element	OxState	*x*	*y*	*z*
Ag/K/Na	+1	0.7149	0.2438	0.1204
Ag/K/Na	+1	0.2732	0.7585	0.3728
Nb	+5	0.2232	0.2565	0
Nb	+5	0.2292	0.254	0.2502
O	-2	0.0506	0.541	0.0054
O	-2	0.5186	0.0327	0.4868
O	-2	0.0358	0.0331	0.2645
O	-2	0.4603	0.5364	0.2299
O	-2	0.2262	0.3124	0.3727
O	-2	0.2649	0.1871	0.1229

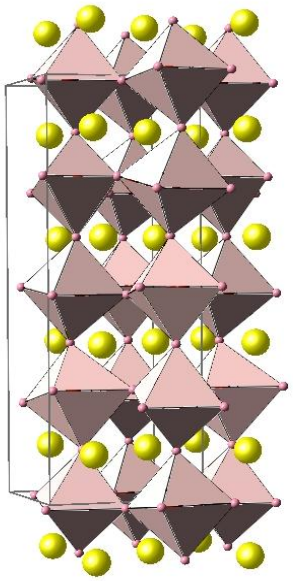

Figure 4.9: Schematic view of the polar structure of 0.80AN-0.20KNN solid solution with orthorhombic space group $Pbc2_1$. Big yellow and small pink balls denote silver/potassium/sodium, and oxygen ions, respectively. The Nb^{5+} ions are inside the pink oxygen octahedrons.

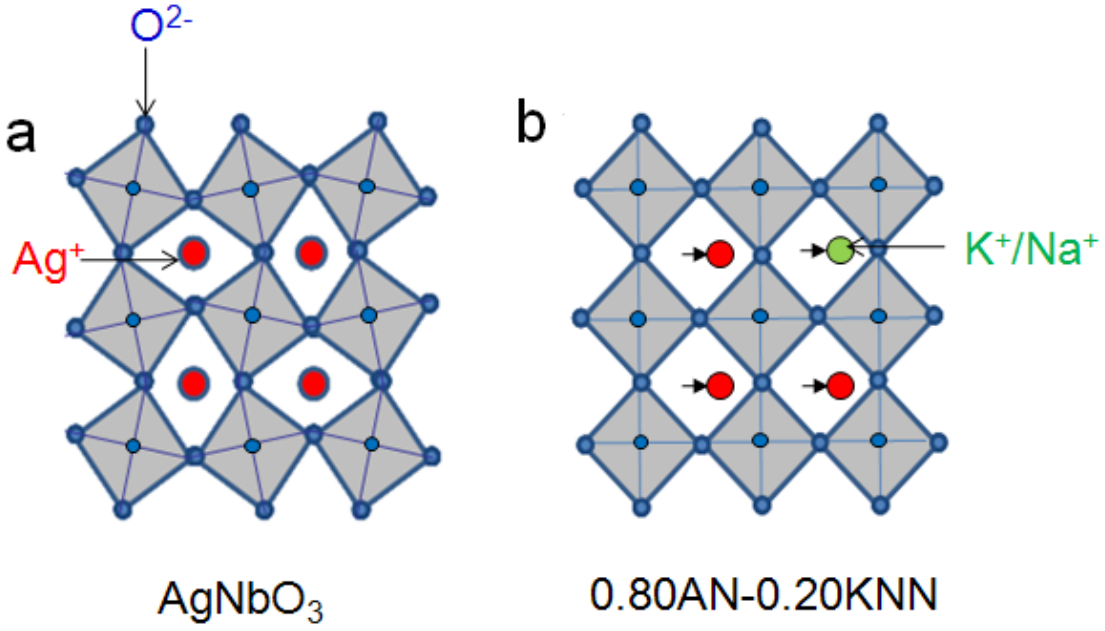

Figure 4.10: (a) Projection of a layer of tilted octahedrons in $AgNbO_3$. (b) Projection of one layer of octahedral in the ideal structure of normal ferroelectric.

4.4.6 Structure-Property Phase Diagram of the (1-*x*)AN-*x*KNN Solid Solution

Based on the results obtained from the dielectric, ferroelectric, and pieozoelectric measurements, and the structural refinement, a structure-property phase diagram of (1-*x*)$AgNbO_3$-*x*$K_{0.5}Na_{0.5}NbO_3$ solid solution was constructed, as shown in Figure 4.11. The data on the KNN side (composition $x > 0.60$) of the solid solution are obtained from C. Lei (2008) [16].

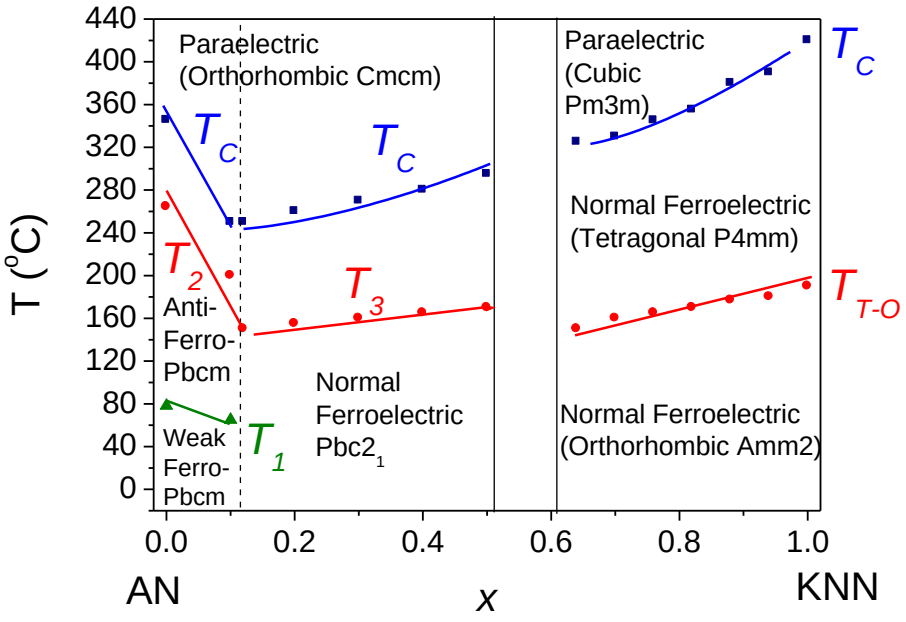

Figure 4.11: Structure-property phase diagram of the (1-*x*)AN-*x*KNN solid solution. T_C, T_{T-O}, T_1, T_2, and T_3 indicate the Curie temperature, the phase transition temperature between tetragonal and orthorhombic phases, the phase transition temperature between orthorhombic M_1 and M_2 phases, the phase transition temperature between orthorhombic M_2 and M_3 phases, and the new phase transition temperature for $x \geq 0.12$, respectively. The solid lines indicate the limit of

solid solution. The dashed line indicates the phase boundary between weak ferroelectric and normal ferroelectric phases. The data on the KNN side ($x > 0.60$) of the solid solution are obtained from C. Lei (2008) [16].

In the phase diagram, the phase boundaries and phase transition temperatures are indicated in this solid solution system. Initially, pure AN exhibits a weak ferroelectric/antiferroelctric phase transition at 78^{o}C. As the KNN-content increases, this phase transition temperature is reduced gradually. When the KNN-content is above 12%, the weak ferroelectric/antiferroelctric phase transition is completely suppressed, as indicated by the enhancement of ferroelectric and piezoelectric properties as well as a refined polar structure. The room temperature weak ferroelectric phase is transformed into a normal ferroelectric phase. This structural phase transition can also be clearly evidenced by the variations in lattice parameters in Figure 4.2. Compared with the data on the KNN side [16], the increases of T_3 and T_C with increasing KNN-content for the composition of above 12% show the similar trend as the $T_{T\text{-}O}$ and T_C in KNN rich side of the solid solution ($x > 0.60$). This suggests that the ferroelectric phases on the both sides of the solubility gap could have the same nature, and the symmetry of high temperature phase between T_C and T_3 on the AN side could be tetragonal. Further structural analysis is required to confirm the symmetry.

4.5 Conclusions

The ceramics of a new solid solution of (1-*x*)AN-*x*KNN have been synthesized by solid-state reaction under oxygen atmosphere. The dielectric, ferroelectric, and piezoelectric properties of these ceramic samples have also been investigated. The substitution of the complex $(K_{0.5}Na_{0.5})^+$ ion for Ag^+ ion shifts T_C toward a lower temperature from 345 ^oC for $x = 0$ to 250 ^oC for $x = 0.1$. T_C increases again from 250 ^oC to 280 ^oC for $x = 0.12$-0.40. The maximum dielectric constant has increased significantly with the increase of the $(K_{0.5}Na_{0.5})^+$ content, i.e. ~ 8.5 times higher for $x = 0.12$ than for the pure AN. Moreover, a saturated hysteresis loop with a maximum remnant polarization $P_r = 6.5\ \mu C/cm^2$ is found at room temperature in the ceramic with the composition $x = 0.30$. This large value of the remnant polarization suggests that the weak ferroelectric phase in $AgNbO_3$ is transformed into a normal ferroelectric phase in the (1-*x*)AN-*x*KNN solid solution, as a result of the KNN substitution. It is believed that the substitution of larger A-site ion, $(K_{0.5}Na_{0.5})^+$, suppresses the tilting of oxygen octahedrons in $AgNbO_3$. Moreover, the structural analysis of the 0.80AN-0.20KNN solid solution indicates that the induced ferroelectric phase adopts a non-centrosymmetric and polar group ($Pbc2_1$), which is different from the centro-symmetric and non-polar group (Pbcm) in $AgNbO_3$. The improved dielectric, ferroelectric, and piezoelectric properties of the (1-*x*)AN-*x*KNN

solid solution ceramics offer a promising potential as lead-free ferroelectric materials for memory device applications.

References:

[1] A. Kania, J. Phys. D-Appl. Phys. **34** (10), 1447 (2001)

[2] M. Verwerft, D. Vandyck, V. A. M. Brabers, J. Vanlanduyt, and S. Amelinckx, Phys. Status Solidi A-Appl. Res. **112,** 451 (1989).

[3] A. Kania and S. Miga, Mater. Sci. Eng. B-Solid State Mater. Adv. Technol. **86,** 128 (2001).

[4] K. H. Ryu, J. A. Cho, T. l. Song, M. H. Kim, S. S. Kim, H. S. Lee, S. J. Jeong, J. S. Song, and K. S. Choi, Ferroelectrics **338**, 57 (2006).

[5] A. Kania, Ferroelectrics **205**, 19 (1998).

[6] A. Ratuszna, J. Pawluk, and A. Kania, Phase Transitions **76**, 611 (2003).

[7] M. Pawelczyk, *Phase Transit.* **8** (4), 273 (1987).

[8] Y. Sakabe, T. Takeda, Y. Ogiso, and N. Wada, Jpn. J. Appl. Phys. Part 1 **40,** 5675 (2001)

[9] I. Grinberg, A. M. Rappe, Appl. Phys. Lett. **85** (10), 1760-1762 (2004).

[11] D. S. Fu, M. Endo, H. Taniguchi, T. Taniyama, and M. Itoh, Appl. Phys. Lett. **90,** 3 (2007)

[12] A. Kania, S. Miga, Mater. Sci. Eng. B-Solid State Mater. Adv. Technol. **86** (2), 128 (2001).

[13] M. Kosec, D. Kolar, Mater. Res. Bull. **10** (5), 335 (1975).

[14] R. E. Jaeger, L. Egerton, J. Am. Ceram. Soc. **45** (5), 209 (1962).

[15] H. Birol, D. Damjanovic, and N. Setter, J. Eur. Cera. Soc. **26**, 861 (20060.

[16] C. Lei, Z. G. Ye, Appl. Phys. Lett. **93** (4), 3 (2008).

[17] R. D. Shannon, Acta Crystallogr. Sect. A **32** (SEP1), 751 (1976).

[18] F. S. Galasso, *Structure, Properties and Preparation of Perovskite Type Compounds* (Oxford Eng.: Pergamon, 1969).

[19] A. Kania and J. Kwapulinski, J. Phys.: Condens. Matter. **11**, 8933 (1999).

[20] R. von der Muehll, A. Sadel, and P. Hagenmuller, J. Solid. State. Chem. **51**, 176 (1984).

Chapter 5

General Conclusions and Future Directions

5.1 General Conclusions

Lead-based materials, such as PZT, have been extensively used for electromechanical transducer applications due to their high piezoelectricicity. However, those lead-based materials have a drawback from the viewpoint of environmental protection. Recently, there is an increasing demand to replace PZT with lead-free alternatives. $AgNbO_3$ (AN) is a promising candidate for the ferroelectric applications because of its high Curie temperature. Therefore, the main objective of this Thesis is to design and synthesize AN-based material and to investigate the dielectric, ferroelectric and piezoelectric properties of theses materials in the form of ceramics.

Two parts of research work have been carried out, one on the $(1-x)AgNbO_3$-$xKNbO_3$ (AN-KN) solid solution system and the other on the $(1-x)AgNbO_3$-$xK_{0.5}Na_{0.5}NbO_3$ (AN-KNN) solid solution system

Dense ceramics of both solid solutions with stable perovskite phases were successfully synthesized by solid-state reactions in controlled oxygen atmosphere. The dielectric measurements show that the substitution of K^+ or $(K_{0.5}Na_{0.5})^+$ ions for Ag^+ ion

induces a significant shift in the phase transition temperatures of AN. The results shows that two phase transition at T_1 and T_2 merge into one phase transition at T_3, suggesting the phase transformation of the pure AN has taken place. In addition, it was found that the dielectric constant at room temperature is greatly increased in both systems, which makes these materials useful for potential dielectric capacitor applications. More interestingly, the piezoelectric and ferroelectric properties of the (1-*x*)AN-*x*KN and (1-*x*)AN-*x*KNN ceramics have also been improved significantly compared to the pure AN ceramics. This is explained by the transformation from the weak ferroelectric phase in AN into a normal ferroelectric phase with enhanced polar order in the solid solution. The crystal structural analysis of 0.80AN-0.20KNN confirms that the initial centrosymmetric and nonpolar phase (Pbcm) of AN has been transformed into a non-centrosymmetric and polar symmetry $Pbc2_1$. Such a chemically induced ferroelectric phase transition arise from the elimination of oxygen octahedral tilting following the substitution of K^+ or $(K_{0.5}Na_{0.5})^+$ for Ag^+ ion, which unlocks the long-range ferroelectric order. This approach is expected to be applicable to other weak-ferroelectric or non-ferroelectric systems. The normal ferroelectric order in these systems can be induced via appropriate chemical substitutions in order to enhance their dielectric and ferroelectric properties. The results obtained in this work provide a better understanding of the relationships between the structure and

properties of the AN-based solid solutions. On the other hand, the enhanced dielectric, ferroelectric, and piezoelectric performances found in these solid solution systems entitle them a new class of lead-free ferroelectric materials, potentially useful for a wide range of applications as high energy density capacitors, electromechanical transducers, and non-volatile memory devices.

5.2 Future Directions

As in the cases of almost all the lead-free materials so far reported, the ferroelectric and piezoelectric properties of the (1-*x*)AN-*x*KN and (1-*x*)AN-*x*KNN ceramics are still not as good as PZT ceramics. In order to further improve their performance, it is necessary to grow single crystals of these two solid solutions. Various growth techniques need to be developed, such as the high-temperature solution (flux) method and top-seed solution growth. Characterization of the single crystals of these systems will help understand the intrinsic physical properties of these materials.

Finally, high temperature structural analysis of AN-KN and AN-KNN ceramics needs to be performed in order to establish the complete phase diagram. This can be realized by using a high temperature x-ray diffraction technique, which will allow us to refine the structure at high temperature thus identifying the symmetry of the phase. Since

the phase transition in these systems involves subtle changes in atomic positions and octahedral arrangement, it will be useful to further expand the structural study by using synchrotron XRD. Synchrotron XRD gives more accurate measurement of the structure and lattice parameters, which allows us to have better understand of the molecular mechanism of the induced ferroelectric phase.